Matter Article

Chiroptical detection and mutation analysis of cancer-associated extracellular vesicles using microfluidics with oriented chiral nanoparticles

Graphical abstract

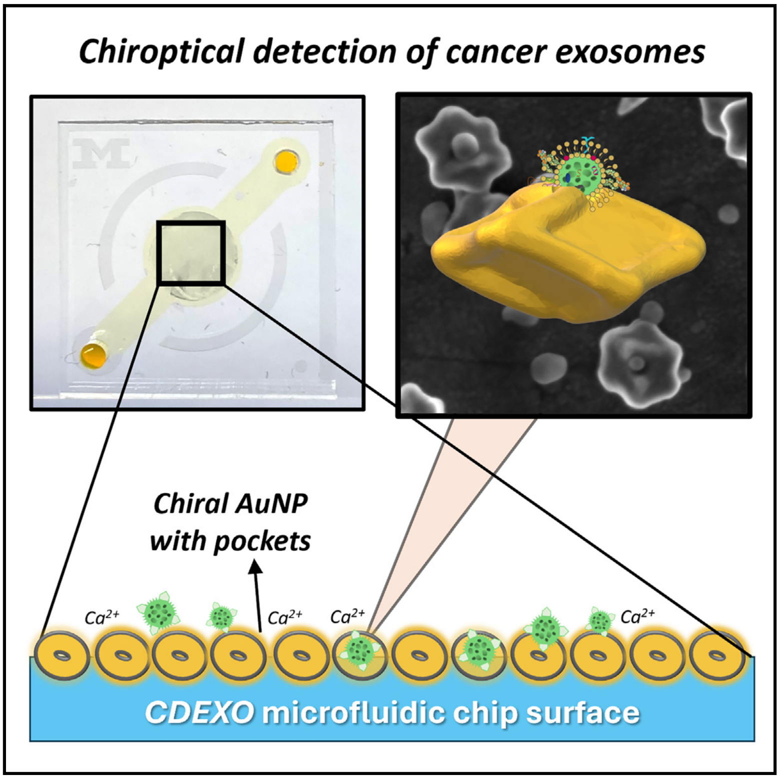

Highlights

- Circular dichroism spectroscopy is inherently suitable for exosome profiling
- Gold nanoparticles with twisted disk geometry are assembled onto a microfluidic device
- The CDEXO chip rapidly isolates and detects tumor-derived exosomes from plasma
- Chiroptical sensing enables profiling of exosomes with mutation specific surface proteins

Authors

Yoon-Tae Kang, Ji-Young Kim,
Emine Sumeyra Turali-Emre, ...,
Nithya Ramnath, Sunitha Nagrath,
Nicholas A. Kotov

Correspondence

yoontae.kang@gmail.com (Y.-T.K.),
kimj58@rpi.edu (J.-Y.K.),
snagrath@umich.edu (S.N.),
kotov@umich.edu (N.A.K.)

In brief

The CDEXO chip utilizes chiral gold nanoparticles assembled as thin films within a microfluidic chip, allowing for the direct isolation and analysis of cancer-specific exosomes from blood plasma. The nanoparticles exhibit marker-specific chiroptical responses, which help in profiling cancer exosomes. Exosomes from lung cancer patients can be distinguished from those from healthy donors based on molecular chirality. The observed dependence of plasmonic resonances on specific mutations will enable rapid, direct, and in-line mutation/deletion analysis.

6 **Development**
Practical, real world, technological considerations and constraints

Kang et al., 2024, Matter 7, 4373–4389
December 4, 2024
Published by Elsevier Inc.
https://doi.org/10.1016/j.matt.2024.09.005
CellPress

Matter

CellPress
OPEN ACCESS

Article

Chiroptical detection and mutation analysis of cancer-associated extracellular vesicles using microfluidics with oriented chiral nanoparticles

Yoon-Tae Kang,[1,8,*] Ji-Young Kim,[1,2,4,8,*] Emine Sumeyra Turali-Emre,[1] Abha Kumari,[1] Hee-Jeong Jang,[1] Minjeong Cha,[1] Colin Palacios-Rolston,[1] Chitra Subramanian,[1] Emma Purcell,[1] Sarah Owen,[1] Chung-Man Lim,[1] Rishindra Reddy,[5] Shruti Jolly,[6] Nithya Ramnath,[7] Sunitha Nagrath,[1,3,9,*] and Nicholas A. Kotov[1,2,*]

[1]Department of Chemical Engineering and Biointerfaces Institute, University of Michigan, Ann Arbor, MI 48109, USA
[2]Center for Complex Particle Systems (COMPASS), University of Michigan, Ann Arbor, MI 48109, USA
[3]Roger Cancer Center, University of Michigan, Ann Arbor, MI 48109, USA
[4]Department of Chemical and Biological Engineering, Rensselaer Polytechnic Institute, Troy, NY 12180, USA
[5]Michigan Medicine Thoracic Surgery Clinic, Ann Arbor, MI 48109, USA
[6]Radiation of Oncology, University of Hospital, University of Michigan, Ann Arbor, MI 48109, USA
[7]Department of Internal Medicine, University of Michigan, Ann Arbor, MI 48109, USA
[8]These authors contributed equally
[9]Lead contact
*Correspondence: yoontae.kang@gmail.com (Y.-T.K.), kimj58@rpi.edu (J.-Y.K.), snagrath@umich.edu (S.N.), kotov@umich.edu (N.A.K.)
https://doi.org/10.1016/j.matt.2024.09.005

PROGRESS AND POTENTIAL Conventional antibody-based exosome cargo analysis requires large amounts of exosomes as well as lengthy multistep procedures. In addition, isolation of cancer-associated exosomes directly from blood plasma is challenging due to their heterogeneity and limited isolation technologies. In this study, we present a microfluidic device with a layer-by-layer assembly of chiral gold nanoparticles that affords sensitive detection of lung cancer-associated exosomes directly from blood plasma. Exosomes from lung cancer patients can be distinguished from those from healthy donors by chiroptical spectroscopic signatures of exosomal biomolecular components, further enhanced by chiral plasmonic nanoparticles deposited in the device. The developed spectroscopic metrics will provide faster and reliable tests for certain cancer-associated receptors than traditional techniques, which will open the broad utilization of exosomes for disease diagnosis.

SUMMARY

Cancer-cell-secreted small extracellular vesicles, known as exosomes, represent a rapidly emerging family of cancer biomarkers. However, the current protocols for exosome analysis require complex equipment and lengthy procedures, which prevents their broad utilization for cancer diagnosis. We have engineered plasmonic gold nanoparticles combining molecular and nanoscale chirality, and have demonstrated that such nanoparticles in self-assembled films in a microfluidic device can isolate and analyze exosomes directly from blood plasma due to marker-specific chiroptical responses and volumetric electromagnetic resonance. Cancer exosomes can be distinguished from those from healthy donors by their giant polarization rotation signatures, and the observed dependence of plasmonic resonances on mutations of epidermal growth factor receptor suggests the possibility of in-line mutation/deletion analysis of protein cargo based on molecular chirality. The present microfluidic chips eliminate ultracentrifugation and improve the sensitivity and detection speed by at least 14 times and 10 times, respectively, enabling the rapid liquid biopsy of cancer.

INTRODUCTION

Most cells secrete 30- to 1,000-nm extracellular vesicles (EVs) that carry informative cargo containing proteins, lipids, and nucleic acids[1] and play essential roles in cell-cell communications.[2,3] The cargo and membrane proteins of small EVs with diameters of 30–200 nm (sEVs), often referred to as exosomes, reflect the biological activity and status of malignant cells by which they were secreted,[4,5] playing an important role in cancer progression and metastatic destination.[6,7] Recently, it was also shown that exosomes carry the mutated proteins reflective of their cellular origin,[8,9] prompting their ongoing studies as prominent biomarkers for cancer diagnostics. However, conventional antibody-based methods of exosome cargo analysis, such as western blot and enzyme-linked immunosorbent assay (ELISA), require large amounts of EVs. Multistep purification processes involving ultracentrifugation followed by marker enrichment represent the key threshold for the use of exosomes and other EVs for liquid biopsies.[10–12] As recent studies demonstrate, ultracentrifugation of exosomes suffers from operational complexity, lengthy process, low purity, and poor reproducibility,[13–15] which prevents their broad utilization and timely disease diagnosis. The need for large sample volumes of body fluids, such as blood, also makes it difficult on patients.

Microfluidic technologies have been used for exosome analysis in a limited capacity and with varying degrees of success.[16–18] Recent advances in optical components for microfluidic systems led to improvements in their detection limit and information content.[19,20] For example, a surface plasmon resonance (SPR)-based analytical method offered label-free and high-sensitivity optical detection of exosomes using a gold-coated glass slide[21] or functionalized titanium nitride layer.[22] Surface-enhanced Raman scattering (SERS) offered signal amplification and real-time detection capabilities,[23,24] as exemplified by the detection of immune checkpoint molecules[25] and cancer exosomes.[26–28] However, the relatively low optical cross-section and non-linearity of SERS[29–31] necessitate considerable sample pre-processing and data post-processing. Like conventional protein profiling methods, these additional steps make the process lengthy and impose clinical limitations. Concurrently, a microfluidic platform capable of exosome capture can also be utilized for SPR assay using periodic nanohole arrays.[32] These substrates, however, require a sophisticated fabrication process and are difficult to implement in inexpensive devices.[23,33] While studies on Raman scattering, nanohole arrays, and non-linear plasmonic effects[34,35] represent extensive progress, rapid antibody-free detection of protein markers on exosomes using low-volume blood samples remains as desirable and difficult as before.

Circular dichroism (CD) spectroscopy can help uncover a rich information content of exosomes. Chirality is omnipresent in biomarkers, and multiscale chirality and enantiomeric preferences of biological molecules can reveal disease states and physiological conditions. For instance, the enantiomeric ratio of certain metabolites aids in diagnosing diseases and monitoring treatment effectiveness, thereby enhancing the accuracy and specificity of medical diagnostics.[36] CD spectra reflecting the multiscale chirality of optically active particles at different spectral characteristics[37] are sensitive to minute changes in the conformation of biomolecules. They are also attractive for exosome analysis. The information about membrane, composition heterogeneity, and exosome cargo can be potentially deciphered from polarization rotation of light.[38,39] However, CD spectra are typically weaker than the standard UV-visible (UV-vis) spectra. Furthermore, the CD activity of other components of biological media[40] (i.e., proteins, lipids, sugars) overlaps with exosomes. Many researchers found that plasmonic nanostructures can enhance CD peaks from biomolecules due to their giant chiroptical activity and resonance coupling with specific energy levels. Additionally, plasmonic particles can shift CD peaks to the red and near-infrared wavelengths, where the interference from non-specific components of biological media is minimal.[34,35,41,42] The ability of biological nanostructures to interact with chiral inorganic nanoparticles (NPs) drastically improves limits of detection for high-molecular-weight biomolecules,[43–45] including protein disease markers.[46,47]

Thus, we hypothesized that cancer-associated exosomes with chiroplasmonic NPs could be identified by their polarization signatures. We experimentally show that microfluidic chips designed for the CD detection of exosomes (CDEXO) make possible rapid and robust detection of cancer-derived exosomes and, more generally, sEVs using gold (Au) NPs shaped as a twisted disk with a central cavity. We chose Au NPs due to their strong plasmon resonances, especially in the visible and near-infrared regions of the electromagnetic spectrum, which enables the utilization of inexpensive lasers and scalable optical substrates for CDEXO chips. The sub-100-nm pockets in the center of the NPs matches exosome dimensions. The electromagnetic resonances encompassing the entire volume of sEV diameters captured in the pocket and uniform orientation of the NPs parallel to the substrates (Figure 1) collectively enable accurate detection of cancer-associated exosomes directly from plasma without ultracentrifugation. The in-depth analysis of the CD spectra also indicates the possibility to distinguish different mutations of protein markers carried by exosomes. While the origin and limitations of such mutation selectivity will still need to be elaborated further, these findings open the path to exosome-based liquid biopsies taking advantage of the versatility of chiral NPs and low cost of microfluidic chips.

RESULTS

Overview of performance-critical features of exosome-specific CDEXO analysis

The high performance and simplicity of the engineering of the CDEXO chips rest on the multiscale optimization of the NPs specifically for exosomes. First, the disk-like shape of the NPs engenders uniform face-to-face self-assembly on the substrate,[48] which facilitates both chip manufacturing and exosome capture. Second, the alignment of helical axes of adsorbed twisted disks with light-propagation direction maximizes the chiroptical response of their nanoscale complexes with exosomes. Third, the geometric complementarity between the sub-100-nm central pocket in NPs and the strong electric field within this cavity is optimal for chirality-specific plasmonic resonances with exosomes of similar size. It is also noteworthy that the dynamic nature of biomolecular interactions favors the formation of molecular-scale adducts between components with stronger short-range attractive interactions, and thus exosomes can easily displace proteins, protein-protein agglomerates, and apolipoprotein agglomerates present in blood.[49] Fourth, NPs were modified with Annexin V, known for strong cooperative interactions with phosphatidylserine (PS) enriched in cancer-associated exosomes.[50,51] High affinity between PS and Annexin V reduces both time and sample loss compared to previously used isolation methods. The next sections provide experimental and computational details of these features.

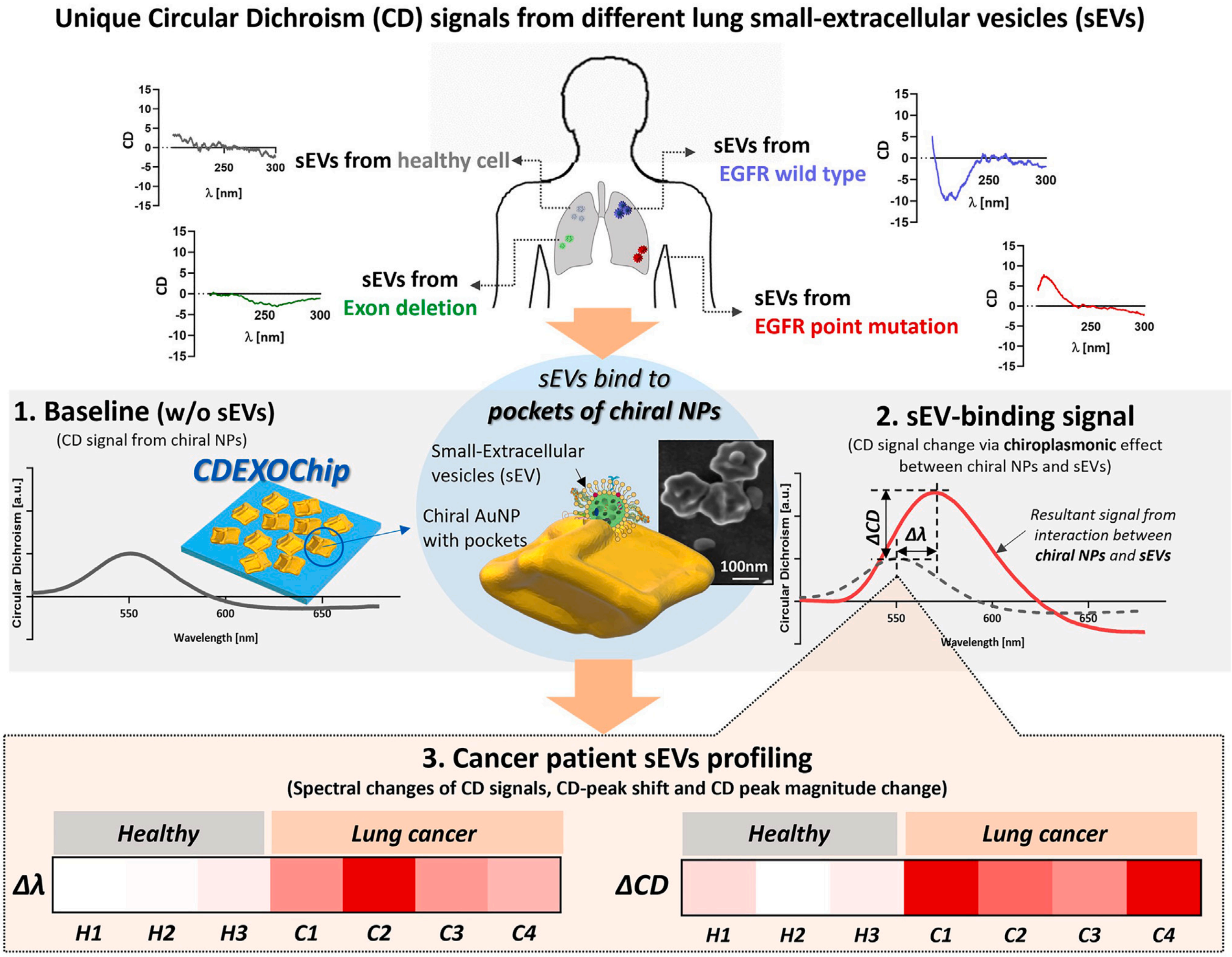

Figure 1. Chiroptical detection and analysis of small extracellular vesicles (sEVs, exosomes) for liquid biopsies

The workflow for profiling of circular dichroism (CD) that affords detection of exosomes from lung cancer cells using a microfluidic device. Exosomes from normal lung cells and lung cancer cells have their unique CD spectra under CD spectroscopy. Their own signal further interacts with chiral NPs (1. Baseline) deposited on the microfluidic device, thus resulting in CD signal change (2. sEV-binding signal). These signal changes are further utilized to differentiate specific cancer patients from healthy donors (3. Cancer patient sEVs profiling).

Synthesis and properties of chiral nanoparticles

The synthesis of chiral NPs was performed using seed-mediated growth starting from Au triangular nanoplates. Chiral features on these initial NPs were grown by reducing an Au^{3+} salt precursor in the presence of L-ascorbic acid, L-cysteine (L-cys) or D-cysteine (D-cys),[52] and cetyl trimethyl ammonium bromide, resulting in NPs shaped as twisted disks (Figures 2A and 2B). L-cys imparts clockwise or left-handed mirror asymmetry, while D-cys yields NPs with a counterclockwise, i.e., right-handed sense of rotation. Both enantiomers display nearly identical ζ-potential and hydrodynamic diameters (Figure S1). They also have the same UV-vis absorbance spectra, while their CD spectra were nearly perfect mirror images of each other with respect to the abscissa of the graphs (Figures 2C, 2D, and S2). The chiroptical properties of NPs were simulated to detail the origin of peaks in the CD spectra. Using the methodology developed previously,[53,54] the three-dimensional (3D) shapes of NPs observed by electron microscopy (Figure S3) were directly imported into a 3D model in the finite element analysis (FEA) computational environment for calculation of their optical properties (Figure S4). The calculated CD spectra matched well with the experimentally observed chiroptical bands for both its spectral range and signs. The chiroptical activity of NP films deposited on the surfaces of the microfluidic channel of the CDEXO chips that was calculated using a particle model with the fixed angle to the substrate also matched the experiments (Figures 2E and 2F).

Microscopy data (upper inset in Figures 2A and 2B) indicate that the central cavity in the NPs facilitates binding of exosomes with nanoscale dimensions to them. In addition, NPs were also modified with phosphatidylserine (PS) due to recently proven high affinity of PS to Annexin V present in many exosomes (Figures 3 and 5).[50,51] NP exploiting PS-Annexin V supramolecular

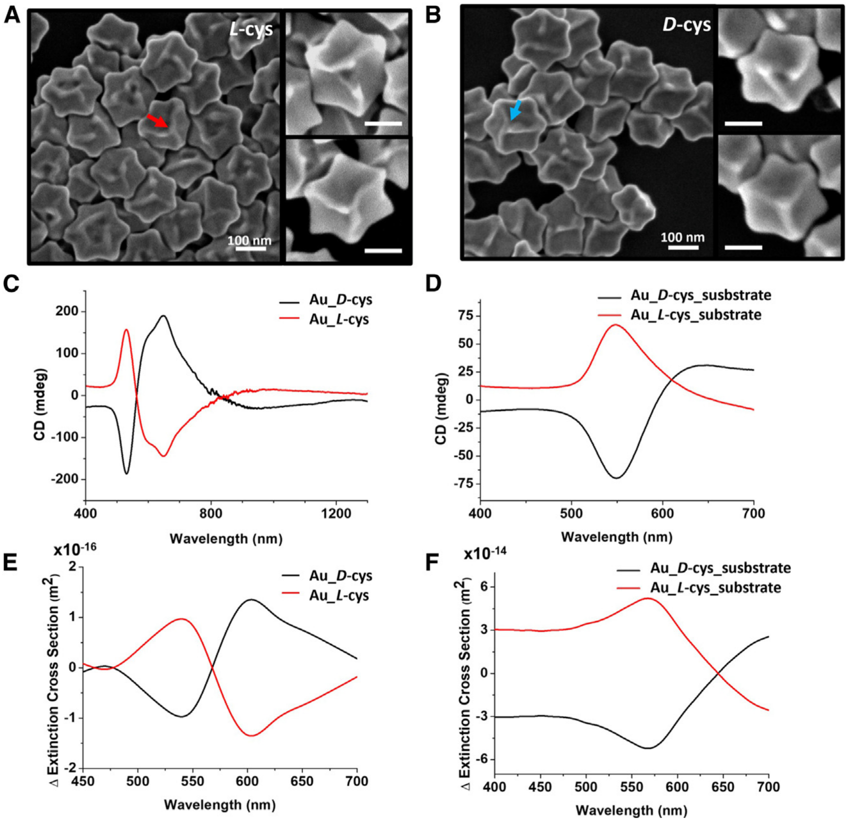

Figure 2. Geometry and optical properties of chiral NPs for exosome detection

(A and B) Scanning electron microscopy (SEM) images of NPs on the substrate synthesized with (A) L-cys and (B) D-cys as surface ligands. Magnified images (inset) show the handedness of the intermediate (upper) and final (lower) structure of the NPs. Scale bars, 100 nm.

(C) CD spectra of colloidal chiral NPs synthesized with L- and D-cys.

(D) CD spectra of chiral NPs deposited on glass substrates used for exosome sensing in CDEXO chips.

(E and F) Difference in extinction cross-section ($\Delta\sigma$) under left-handed and right-handed circularly polarized light ($\sigma_{LCP} - \sigma_{RCP}$) calculated from the model (Figure S3) for random orientation (E) and fixed orientation (F) of NPs in dielectric media in water and air, respectively.

affinity is also expected to reduce both time and sample loss compared to previously used isolation methods.

Geometry of chiral nanoparticles

The chiral NPs can have "pockets" in their central part (Figure 4B); the diameters of these pockets can be controlled by the incubation time for the growth step (Figure S6).[51] Noteworthy is that they are concave, not cylindrical, and thus can capture exosomes. The maximum size of exosomes that can be captured by these concave areas can be estimated by calculation of specific geometrical characteristics of pocketness and minimum inaccessible radius (Figures 5D and 5E, respectively). The central cavities with diameters of 27–64 nm in NPs can capture exosomes with diameters up to ~120 nm (Figures 5E and S7), which is confirmed by scanning electron microscopy (SEM) images indicating that the exosomes are indeed localized predominantly within these concave areas (Figure 5B). Scanning transmission electron microscopy (STEM) elemental mapping of phosphorus, which is specific to exosome membrane, confirmed exosome binding to these pockets (Figures 4C–4E). Elemental mapping analysis of surface-modified chiral NPs and exosomes was also demonstrated to reveal their own unique element profiles (Figures S13 and S14). The phosphorus peaks are localized exclusively in the concave area. If exosomes are small enough, more than one exosome can fit into the area (Figure 4D), resulting in two peaks in the STEM profile for phosphorus. We also found that the central cavities on the NPs display higher affinity to the thiol-containing molecules (Figures 4C–4E), which leads to higher density of immobilized Annexin V molecules in them and, thus, to the preferential affinity of the exosomes to this region on the NP surfaces.

Chiroplasmonic resonances of the nanoparticles

The chiroptical properties of NPs and their nanoscale complexes with exosomes were simulated to detail the origin of peaks in their CD spectra. Using the methodology developed previously,[53,54] the 3D shapes of NPs observed by electron microscopy (Figure S3) were directly imported into a 3D model in the FEA computational environment for calculation of their optical properties (Figure S4). The calculated CD spectra of the NPs matched well the experimentally observed chiroptical bands. The same was true for NP films deposited on the surfaces of the microfluidic channel (Figures 2E and 2F). Importantly, the illumination in the direction normal to discoidal particles resulted in the strong localization of the electric field in the central cavity (Figures 5F–5H and S10). The plasmonic resonance resulted in a "hot spot" that engulfed the entire sub-100-nm pocket. This unique feature made it possible to probe the entire exosome nested there, which maximizes the analytical capabilities of the chips. Also important, the electrical field is very much stronger when the helicity of the photons matches the helicity of the particle, improving the chirality-related spectral selectivity (Figure S11).

CDEXO chip design for exosome capture and sensing

The CDEXO chips have one inlet, one outlet, and a sensing region where NPs are deposited (Figures 3A and S5). We used a layer-by-layer (LBL) assembly[55–58] to deposit NPs onto the glass surface of the device because this method affords uniform coating regardless of the complexity of the geometric shapes of the substrate (Figure 3C).

SEM demonstrated that NPs are spread across the device's surface with minimal aggregation with distinct dominance of

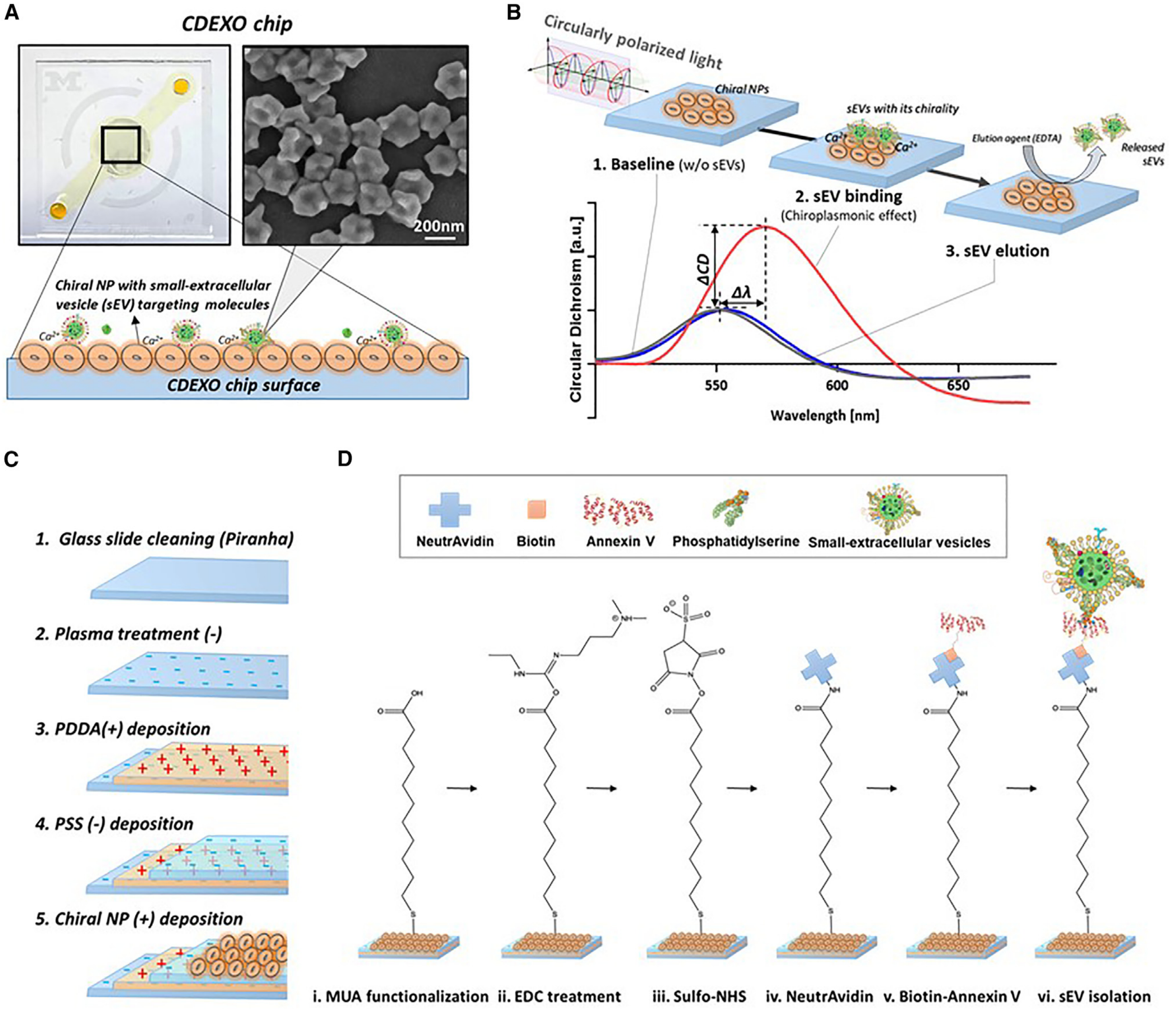

Figure 3. Circular dichroism-based exosome sensing chip for sEV profiling

(A) Engineering design of the microfluidic chip and the schematic of principle of exosomes binding to Au NP films in the CDEXO chip.

(B) Changes in optical properties of chiral Au NP films resulting from exosome binding quantitatively measured through spectral shifts ($\Delta\lambda$) and magnitude changes (ΔCD) in circular dichroism spectra.

(C) Preparation of the NP layer via LBL deposition. A layer of positively charged chiral NPs is deposited on top of a layer of anionic polystyrene sulfonate layer on the glass surface of the CDEXO chip.

(D) Surface modification of chiral Au NPs for exosome isolation using standard 1-ethyl-3-(3-dimethylaminopropyl)carbodiimide and *N*-hydroxysuccinimide chemistry.

planar orientation of the central cavities due to LBL deposition (Figure 4A). The alignment of the asymmetric planar NPs is parallel to the substrates,[59] which makes an essential contribution to the specificity of the spectroscopic readout due to the alignment of the twist axis with *k*-vector of the light beam. Also, geometric alignment of the disk-like NPs with the surface facilitates the entry of exosomes into the central cavity of the chiral particles. The nanoscale roughness of the films with and without exosomes leads to enhancement of the roughness. In both cases the slip-boundary conditions for laminar flow in microfluidics become valid for longer as demonstrated recently in several studies.[60] The nanoscale roughness enhances the mass transfer to the channel surface, as was demonstrated for microfluidic chips for SERS detection.[61]

The CDEXO chips are engineered to slide into a holder of conventional CD instruments (Figure 3B), placing the sensing region directly into the beam path. Captured exosomes strongly change the characteristic bisignate CD peaks of chiral NPs resulting in spectral shift ($\Delta\lambda$) and a magnitude change (ΔCD) (Figure 3B), serving as a spectroscopic identifier of the biomarkers.

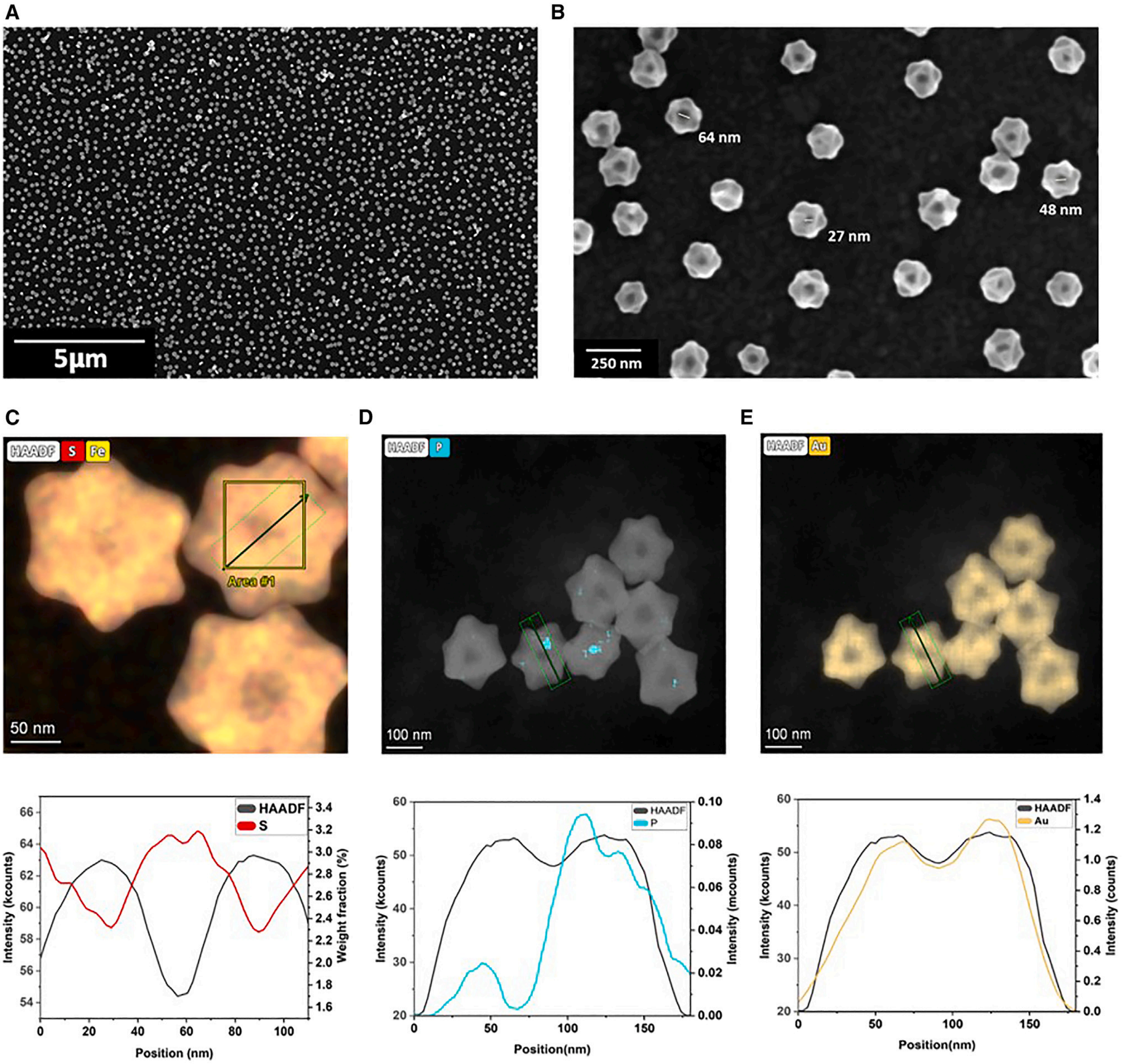

Figure 4. Characterization of chiral Au NPs and their binding of exosomes

(A and B) SEM images of chiral Au NPs deposited in CDEXO chips via LBL assembly. (A) Low-magnification image shows uniform distribution of Au NPs. (B) High-magnification image of the NPs with dimensions of the central pocket.

(C) Element mapping of Au NPs after MUA treatment (top) and its profile within the green box for sulfur (S, red) and high-angle annular dark-field (black) intensity.

(D and E) Elemental mapping of Au NPs with captured sEVs (top) and their profiles (bottom) within green boxes for elements: (D) phosphorus (P, blue) and (E) gold (Au, yellow). HAADF intensity is plotted in black.

Characterization of exosomes derived from different cell lines

Four different sources of exosomes, secreted from normal lung fibroblasts (MRC5), lung cancer cells with wild-type epidermal growth factor receptor (EGFR) (A549), lung cancer cells with exon 19 deletion (H1650), and lung cancer cells with EGFR L858R point mutation (H3255), were used for an initial evaluation of the CDEXO chips for exosome isolation and profiling (Figure 6A). In parallel, the same samples were analyzed using western blot analysis. As expected, all exosomes from the different cell lines displayed CD9 protein (Figure S15), a widely used exosome marker. Using two variants of a lung cancer-associated protein, total EGFR and L858R mutant EGFR, we confirmed that only two of the cancer cell-derived exosome samples express EGFR, and the L858R mutation is associated explicitly with H3255

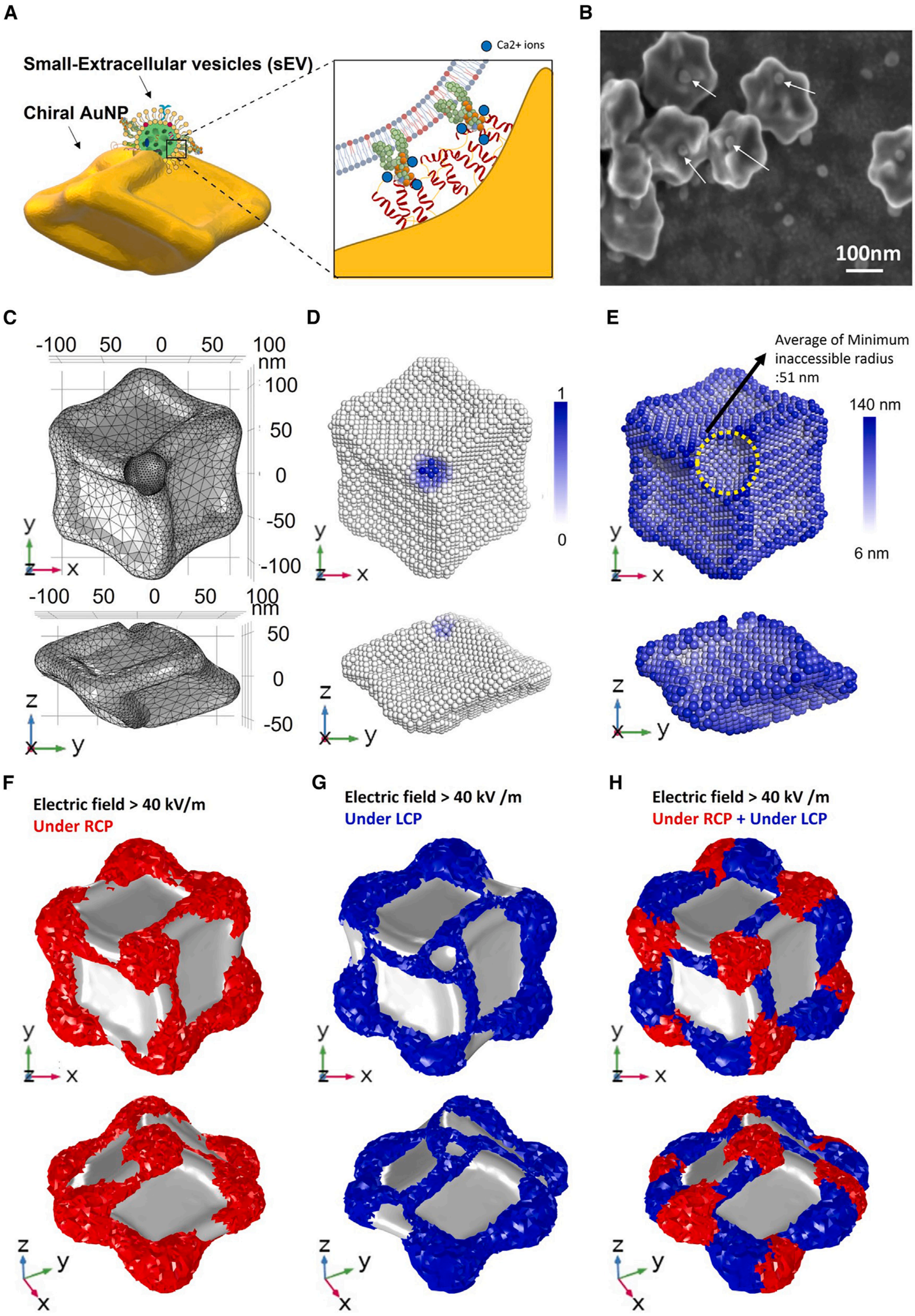

(legend on next page)

cell-derived exosomes, which the cells are known to carry (Figure S15).

The CD spectra of exosomes in water (Figure 6B) for the region between 200 nm and 300 nm give information about different types of secondary protein structures and showed substantial differences. For example, exosomes derived from A549, wild-type EGFR, contain a large density of α helices, whereas exosomes derived from H3255, which shows L858R EGFR mutation, contain a large portion of segments of random coil structures. We note that, based on the CD spectra for the normal lung fibroblasts, MRC5, and the lung cancer exosomes from H1650 with exon 19 deletion, the tested exosomes for cancer cell lines have specific chiroplasmonic signatures potentially derived from heterogeneous exosomal protein expression on their surface.

The fraction of exosomes from spiked dispersions quantifies capture efficiency (Figure 6C) of the cancer-associated exosomes by the NPs. Nanoparticle-tracking analysis (NTA) was used to evaluate size distribution and exosomal concentration (as assessed by the size of exosomes in the 30–150 nm range) of samples before and after adsorption. Annexin V-modified NPs capture cancer-associated exosomes more efficiently (82.4%) than those from normal-cell- or healthy-donor-derived exosomes (43.7%). The efficiency of the CDEXO chip capture for cancer-associated exosomes is significantly higher than that for the exosomes derived from normal cells ($p < 0.0001$). These data were confirmed by bicinchoninic acid (BCA) assay quantifying the total protein lysate. The BCA assays show a similar trend with five different sources of exosomes (Figure S16). We also found that the CDEXO chips capture cancer-associated exosomes more favorably and with higher recovery than ultracentrifugation—the gold standard in exosome analysis (Figure S18). We also compared capture performance of the CDEXO chips with NPs and those functionalized with two different antibodies, anti-EGFR-conjugated and Annexin V-conjugated devices, using an identical number of exosomes as input aliquots for the CDEXO chip. While the capture performance of lung fibroblast-derived exosomes are similar between two types of devices with different surface modifications, the Annexin V-based CDEXO chips (79.8%) outperformed anti-EGFR-conjugated CDEXO chips (57.1%) for two different cancer cell-derived exosomes (Figure 6D, left) ($p < 0.0001$ and $p < 0.001$). DiO lipophilic dye-based exosome staining also revealed noticeably stronger fluorescence for H3255-derived exosomes when using Annexin V-based exosome isolation (Figure 6D, right).

The CD peaks from the baseline (Figure 6E) are associated with the capture of cancer cell-derived exosomes, as evidenced from the comparison of the CD spectra for the microfluidic chips made from Annexin V-conjugated NPs (Figure S12). Furthermore, the isolated exosomes can be easily released by EDTA chelation of Ca^{2+}[50,51,62] as the affinity of Annexin V to PS is Ca^{2+} dependent. This finding implies that exosome binding to NPs rather than other processes that may occur on the chip surface, such as irreversible Ca^{2+} independent adsorption to LBL films, leads to a change of CD signatures. The Ca^{2+} effect can also be utilized to increase the accuracy of detection and reusability of the chips.

CDEXO isolation and in-line mutation analysis

A sharp positive increase in positive CD peak and a strong change in the spectral position of the peak maximum in the range of 520–580 nm were observed after flowing exosomes through the devices (Figure 6E). The two well-studied types of exosomes derived from cancerous A549 and H3255 exhibit a distinctly greater shift from the baseline than the exosomes derived from healthy MRC5 cells; note the p value of <0.001 for both cell lines, indicating that the difference between two types of cancer exosomes can be recognized (Figure 6F). By and large, such sensitivity is quite unexpected due to the multiplicity of proteins and other chiroptically active species present in exosomes. Thus, we decided to investigate the initial indication of the possible mutation differentiation by the CD spectra enhanced by chiral NPs. We found that exosomes with exon 19 deletion (from H1650) exhibit a smaller shift from the baseline, being similar to the exosomes from healthy MRC5 cells. Exosomes exhibiting EGFR point mutation are distinguished from the wild type and exon 19 deletion by a stronger peak shift $\Delta\lambda$. Note also that a negative CD peak can also emerge in the presence of exosomes (Figure S17).

Similar to the positive side of the bisignate CD spectrum, the negative CD peak in the 500–550 nm range also revealed a significant increase ($p < 0.001$ in all cases) in its magnitude in response to the capture of exosomes (Figure 6G), which further increases the accuracy and specificity of detection. The change in magnitudes for the negative peaks, ΔCD, normalized against the original magnitudes was much lower for healthy cells compared to those from cancer cell lines. To clarify why specific point mutations in exosomes could cause such radical changes in the CD signals, we calculated protein maps of weighted Osipov-Pickup-Dunmur (wOPD) chirality indices when the chemical nature of the amino acids was included in the asymmetry calculations (Figure S19; the detailed method for calculation can be found in the previous literature[63,64]). While OPD and other pseudoscalar indices have theoretically been predicted to have chiral zeros, the large contribution of the α helices that have simple pathway for reconfiguration through the true achiral state make OPD in this case illustrative of the changes in local handedness and multiscale chirality. The wOPD maps change considerably for all the mutations that should result in the differences in CD spectra when enhanced by the chiral NPs as demonstrated in Figure 6. Even the single point mutation can

Figure 5. Binding of exosome into the size-matching pockets of chiral Au NPs
(A) Schematic diagram of exosome binding in the pockets of chiral Au NPs.
(B) SEM images of NPs after exosomes binding in pocket of NPs.
(C) 3D models of engineered chiral Au NPs for exosome sensing.
(D and E) Calculated pocketness (D) and minimum inaccessible radius (E) of the 3D model of chiral NPs with a 48-nm pocket opening.
(F–H) Volume plots illustrating the high-electric-field region surpassing the 40 kV/m threshold, considering exposure to the right circular polarization (RCP) configuration (F), left circular polarization (LCP) configuration (G), and their combined effect (H).

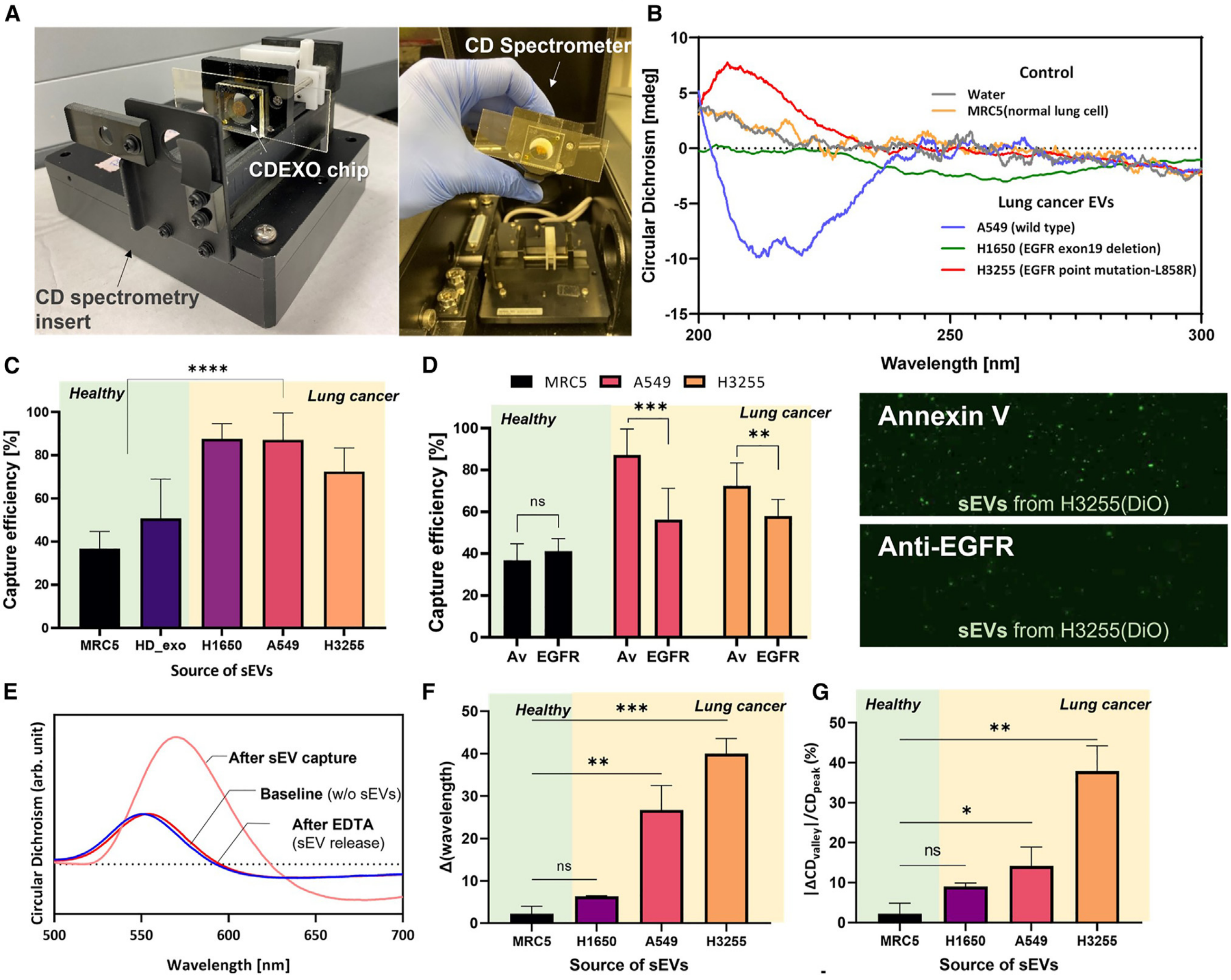

Figure 6. Detection of cancer-associated exosomes using CDEXO microfluidic chips

(A) Photograph of the CDEXO platform for chirality-based exosome analysis.

(B) Characteristic CD spectra of exosomes derived from normal lung and lung cancer cell lines along with controls.

(C) Capture of exosomes from lung cancer cell lines and healthy cells using CDEXO chips ($p<0.0001$).

(D) Exosome capture by chiral NPs coated with Annexin V and anti-EGFR for exosomes from three different sources (left) and DiO-stained exosomes on the devices (right) ($p<0.0001$ and $p<0.001$ for A549 and H3255, respectively).

(E) Changes in CD spectra before and after exosome binding. The peak intensities are reversed after exosome release induced by EDTA in the presence of Ca^{2+}.

(F) CD-peak shift resulted from exosomes derived from four different cell lines analyzed using CDEXO chip ($p<0.001$ and $p<0.0001$ for A549 and H3255, respectively).

(G) Percentage of change in CD-peak magnitude after exosome binding when compared to baseline CD peak ($p<0.01$ and $p<0.001$ for A549 and H3255, respectively).

cause the difference in binding of the proteins and exosomes to the NP surface,[65] which is reflected in the CD spectra. Beyond that, the quantitative use of wOPD for correlation with spectra is not be warranted, and calculations of OPD and wOPD for non-helical segments is not recommended.

We further examined the specificity of the CD spectra to the EGFR-expressing exosomes using a cell line other than a lung cancer line. We used exosomes derived from a glioblastoma (GBM) cell line with an EGFR mutation. The CD spectra of GBM-derived exosomes have nearly identical spectroscopic changes to those of the lung cancer cell line with the similar EGFR mutation associated with the lung cancer (Figure S25). Additionally, the purified wild-type EGFR protein yields CD spectra with band features matching those found in exosomes derived from the wild-type EGFR cell line A549 (Figure S25), which confirms the relationship between chiroptical response and protein mutation.

To quantitatively profile exosome bindings in the same source of exosomes, we analyzed $\Delta\lambda$ and ΔCD at several counts of exosomes between 10^2 and 10^8 per device by serial dilution. Next,

$\Delta\lambda$ and ΔCD were normalized with respect to their respective highest values (Figure S29). Compared to ELISA and similar optical sensing methods that often require more than 10^6 exosome counts per measurement,[32] the CDEXO platform displays higher sensitivity and requires smaller numbers of exosomes per measurement (as few as a few hundred). The limit of detection for our chips was 10^2 exosomes while for real-time PCR it was 10^6, indicating the high sensitivity of the CDEXO assay (Figure S29C) with a detection range from 10^3 to 10^8.

Clinical validation of CDEXO chips in patients with non-small cell lung carcinoma

We analyzed a total of ten healthy control plasma samples and 19 non-small cell lung cancer (NSCLC) patient plasma samples (Figure 7). The comparison of CD peaks from a healthy donor (*HD4*) and those from patients with lung cancer (*LC3*) indicates a distinct increase in ΔCD as well as $\Delta\lambda$ for the positive peak as observed for the cancer patients relative to baselines (Figures 7A and 7B). Lung cancer samples showed greater $\Delta\lambda$ compared to healthy donors ($\Delta\lambda$ = 15.76 vs. 11.45, p = 0.1275); however, there are some lung cancer patients showing minimal change in $\Delta\lambda$ compared to those of the healthy donors. We also evaluated normalized ΔCD_{peak} when CD magnitude changes ($CD_{\text{sEV}} - CD_{\text{initial}}$), ΔCD, are divided by the original magnitudes of each device ($\Delta CD_{\text{peak}}/CD_{\text{initial}}$). In all cases, lung cancer samples showed higher percent changes in ΔCD_{peak} than those of healthy donors (percent change of ΔCD_{peak} = 42.76% vs. 15.63%, p = 0.0037) (Figure S21). Patient identification number-matched profiles can be found in Figure S20. For 14 clinical samples (five healthy and nine lung cancer patient samples), we further released the exosomes after CD signal profiling, and the released samples were quantified and analyzed in terms of concentration and size profiles. This result (Figure S23) showed that over 81% of released samples are in the exosome size range (30–150 nm), while the concentration of exosomes from cancer patients (1.02×10^9/mL) was more than 5.6 times higher than that of healthy donors (1.82×10^8/mL).

Mutation analysis of the plasma exosomes in patients with non-small cell lung carcinoma

After noticing the differences between A549 and H3255 cell lines, we evaluated the possibility of CDEXO detection of at least some EGFR mutations in lung cancer patients. Changes in the CD peaks can be correlated with the EGFR mutations, such as EGFR exon 19 deletion (Figure 7C, left) and exon 21 substitutional point mutations in the EGFR gene (Figure 7C, right), which accounts for 90% of all EGFR mutations. While not replacing full mutation analysis by standard means, the spectroscopic CD signature of EGFR can be a "red-flag" mutation indicator. The ΔCD_{peak} and $\Delta\lambda$ vary between these three cases. As expected from the cell line studies, the samples with EGFR mutation display the negative peak in the 500–550 nm range, which seems to be characteristic of the EGFR exon 19 deletion in the EGFR gene (Figure 7D). Unlike other 12 lung cancer cases, samples with EGFR exon 19 deletion showed minimal peak magnitude change from the baseline (−1.931 vs. 19.81, p = 0.0010). Compared to other cancer cases, the samples having EGFR point mutations have significantly greater values in the percent change for CD_{peak} and CD_{valley} (32.12% vs. 7.829%, p = 0.0031) (Figure 7E). Patient identification number-matched individual profiles can be found in Figure S22. These EGFR mutations have the effect of inducing this large percent increase in negative peak magnitude.

DISCUSSION

Exosomes are emerging as reliable biomarkers given their innate ability to resist degradation in circulation, unlike circulating tumor DNA. Given the excessive exosomes that are present in the blood, it is an unmet need to be able to isolate these with high specificity. The specific isolation of tumor-specific exosomes from the rest of the exosomes in plasma has been a challenge. The technologies with ability to isolate tumor-specific exosomes will transform the future clinical applications of exosomes. The presented microfluidic device with an LBL assembly of chiral Au NPs affords sensitive and accurate detection of lung cancer-associated exosomes from blood plasma due to the central cavity capturing the exosomes, the strong chiroplasmonic field in these cavities enhancing the CD spectra, and uniform in-plane orientation of the NPs on the surfaces further increasing the spectral features. The specificity of exosome binding is enabled by Annexin V-PS affinity combined with the geometrical match with pockets on NPs with the shape of a twisted disk. Another barrier to utilizing the exosomes in a clinical setting is the highly complex downstream assays to profile the tiny cargo that is present within these nanovesicles. While being high in information content, the current protocols for profiling exosomes require complex procedures and equipment involving exosome purification and cumbersome multistep downstream analysis, which prevent their clinical adaptation. There are currently no available methods to distinguish tumor-specific exosomes from normal exosomes (originating from healthy cells) without extensive downstream analysis.

We have also demonstrated that chiral Au NPs when LBL assembled onto a microfluidic device can rapidly isolate and detect cancer-associated exosomes directly from blood plasma without any pre- or post-processing. Our approach of utilizing the microfluidics for the alignment of NPs in the films maximizes both the CD response and exosome capture. Exosomes from lung cancer patients can be distinguished from those from healthy donors by chiroptical spectroscopic signatures of biomolecular components (for, e.g., proteins) of exosomes, further enhanced by chiral plasmonic NPs in one step. Additionally, point mutations and deletion in the EGFR protein were further characterized directly using in-depth analysis of the CD spectra without the need of any downstream processing. While not replacing the full mutation profiling as a part of cancer diagnostics, the spectroscopic signature of EGFR mutations can be an informative screening tool for cancer-derived exosomes. Optically convenient near-infrared resonances of chiral NPs enable in this perspective the low-cost glass/plastic-based microfluidics that represents an attractive pathway for rapid and versatile profiling of EVs. The strong CD peaks benefiting from volumetric plasmonic resonances engulfing the entire exosome nested in

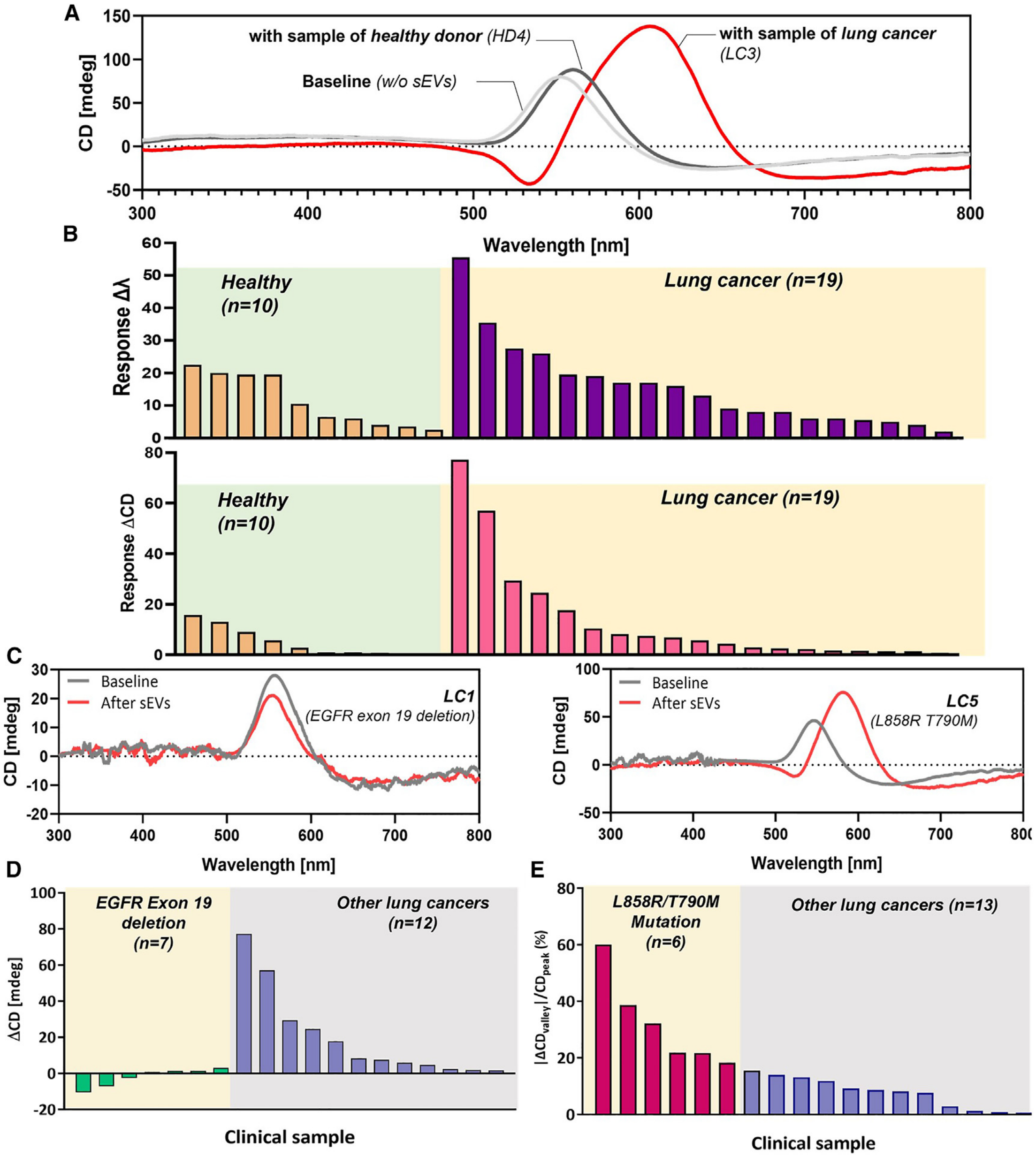

Figure 7. Profiling of lung cancer exosomes from clinical samples

(A) Typical CD spectra of chiral Au NP films in CDEXO chips after adhesion of exosomes from the plasma of a healthy donor and a lung cancer patient.

(B) The magnitude of CD-peak shift (top) and CD-peak magnitude change (bottom) for healthy controls (n = 10) and NSCLC patient samples (n = 19). Each bar represents measurement for each sample.

(C) A typical example of a CD-peak change for a sample with EGFR exon 19 deletion (left) and a sample with both EGFR L858R and T790M mutation (right).

(D) Change in CD-peak magnitude for 19 lung cancer patients, representing the profiles of seven samples with EGFR exon 19 deletion when compared to 12 samples without exon 19 deletion.

(E) Percentage of change in CD-valley magnitude after exosome isolation as compared to baseline CD peak for 19 lung cancer patients with (n = 6) and without (n = 13) any point mutation.

sub-100-nm pockets on chiral NPs facilitate in-line biomedical analysis of sEV cargo including EGFR mutation profiles, enabling rapid real-time liquid biopsy.

The developed spectroscopic metrics may provide faster and more reliable tests for certain cancer-associated receptors in comparison with traditional techniques.[31,66] To this end, future studies should focus on better understanding of the relationships between molecular-scale chirality of carried proteins and chiroptical responses. Implementation of CDEXO analysis in a large clinical study will also be necessary.

Although PS offers the opportunity to isolate the tumor-specific exosomes when compared to the common tetraspanins such as CD63, there is an opportunity to further optimize this by using other tumor-specific markers once it can be established that these markers are present on the membrane of the exosomes. Perhaps having a more specific target can reduce the background signal of exosomes that we observed in healthy controls, thus enhancing the signal readout. The presented technology can be easily adapted to other solid tumors, such as glioblastoma, where the driver mutations in the EGFR play a critical role in disease progression and treatment response. Although our studies are specifically focused on EGFR protein, we expect that chiral NPs can be reconfigured easily to target any other large proteins with the modulation of affinity molecules along with the size and structure of the chiral NPs. The relationships between the chirality measures, point mutations, and CD spectra of NP-exosome complexes can potentially offer high-information-content exosome profiling and merit further evaluation, while CDEXO methodology could be generalized to other tumors and other diseases. Besides the traditional CD spectroscopy, other chiroptical spectroscopies such as Raman optical activity and terahertz CD can also be implemented. We observed varied intensity of signals among the patients. Upon further investigation of the effect of age, stage, and other demographic information (Figure S27), we see some interesting trends, although none reach statistical significance. A larger cohort involving a wider demographic can enable the study of specific effects and the inherent differences observed.

To conclude, chiral Au NPs with twisted disk geometry, multiscale chirality, and scale-appropriate pockets can be implemented for detection and preliminary mutation profiling of lung tumor-specific exosomes. Their further studies will help to underpin the detailed origin of mutation sensitivity and their clinical utility.

EXPERIMENTAL PROCEDURES

Chiral Au NP synthesis

All glassware was pre-treated with aqua regia solution for removal of metal residues and rinsed with deionized (DI) water thoroughly. We prepared Au triangular nanoplates,[67] which are optically normalized for consistent batch-to-batch concentration of NPs. For the preparation of the growth solution, 32 mL of 12.5 mM cetyltrimethylammonium bromide (CTAB), 0.4 mL of 20 mM $HAuCl_4$, 4.0 mL of 0.1 M ascorbic acid (AA), and 0.08 mL of 0.1 mM L-cys (or D-cys) were mixed with a vortex mixer. CTAB, $HAuCl_4$, AA, and L-cys act as a stabilizer, a meter precursor, a reductant, and a chirality controller, respectively. Next, we added 2 mL of Au nanoplate solution into the prepared growth solution to initiate chiral growth on the surface of targeted NPs. All procedures proceeded at 30°C. After 4, 8, 12, and 24 h, the resultant was separated by using a centrifuge and redispersing in DI water. The size of the pocket of particles is decreased with a longer incubation time (Figure S7), and the full-growth particles without a pocket (Figures 2A and 2B) can be obtained with sufficient incubation (24 h).

Zeta-potential and size distribution of chiral NP probes

The ζ-potential and size distribution were measured with a Nano ZS Zetasizer instrument (Malvern Instruments, Malvern, Worcestershire, UK). For ζ-potential, samples were equilibrated for 120 s before each measurement; all measurements were conducted in triplicate, each measurement included 50 cycles, and a 15-s pause was included between runs.

Numerical simulation of optical activity of chiral NPs

Maxwell's equations were solved in the frequency domain by the FEA using COMSOL Multiphysics 5.5 software package (the radiofrequency module). The 3D propeller-shaped disk particles (Figure S4; Videos S1, S2, and S3) were modeled based on the shape and dimensions found from electron microscopic images. The model structures were placed in a homogeneous surrounding medium with an effective refractive index of 1.33 (water) and 1.0 (air) for colloidal and chip samples, respectively. The dielectric functions of Au NPs were taken from the literature.[68] The maximum mesh size of FEA was set to $\lambda/4n$, where λ is the wavelength of incident light and n is the real part of the material refractive index was used to minimize the scattering from the outer boundary. The particles were placed in the x-y plane parallel to their longitudinal axis, while the circularly incident light was propagated along the z axis with port power of 8.1×10^{-5} W. For colloidal particle analysis, the particle structure was rotated with step of $\pi/6$ along with x and y axes, and the averaged extinction cross-sections were obtained to analyze chiroptical response of the model. For analysis of solid chip samples, spectra were calculated at one angle, where the longitudinal axis of particles was normal to incident direction (z), as the model was initially placed.

The model computes the scattering, absorption, and thus extinction cross-sections of the Au NP enantiomers under left circular polarization (LCP) and right circular polarization (RCP) light.

The total scattering cross-section (σ_{sc}) is defined as

$$\sigma_{sc} = \frac{I}{I_0} \iint (n \cdot S_{sc}) dS.$$

Here, n is the normal vector pointing outward from the local surface, S_{sc} is the scattered intensity (Poynting) vector, and I_0 is the incident intensity. The integral is taken over the closed surface of the meta-atom. The absorption cross-section (σ_{abs}) is expressed as

$$\sigma_{abs} = \frac{I}{I_0} \iiint Q dV,$$

where Q is the power-loss density in the structure, and the integral is taken over its volume.

The total extinction cross-section (σ_{ext}) is simply the sum of the scattering and absorption:

$$\sigma_{ext} = \sigma_{sc} + \sigma_{abs}.$$

The chiroptical response of the particles can be characterized as $\sigma_{ext,RCP} - \sigma_{ext,LCP}$.

Fabrication of microfluidic channels for CDEXO chips

The top layer and bottom masking layer of the CDEXO chip is fabricated by standard soft lithography including mold fabrication and polydimethylsiloxane (PDMS) molding. By patterning SU8-2050 photoresist on a silicon wafer, we prepared the top and bottom masking layer molds. The top chamber layer was fabricated by pouring PDMS and PDMS curing agent mix (1:10) (Dow Corning, USA) onto the silicon mold after degassing of PDMS mixture in vacuum for 10 min. The thin masking layer was prepared using a PDMS mixture spun on the silicon mold at 1,000 rpm for 30 s followed by incubation at 70°C for 2 h. The top and bottom layers were cut, punched, and placed for processing of samples.

Chiral NP deposition on glass substrates

A standard slide glass was treated by first piranha solution and incubated overnight to activate negatively charged functional groups on the glass surface. After gentle washing with water and drying procedure, a thin layer of PDMS with openings was attached on the slide glass assisted by an electrostatic binding, followed by deposition of alternative multilayer films of cationic poly(dimethyldiallyl ammonium chloride) (PDDA) and anionic polystyrene sulfonate (PSS). 100-μL droplets of 2 wt % PDDA solution were applied to each opening and allowed to incubate for 1 h at room temperature. The devices were then washed by dipping into four separate tubes of DI water consecutively followed by thorough and careful air drying. Next, 100-μL droplets of 1.8 wt % PSS solution were applied to each opening on the glass slides and allowed to incubate for 1 h at room temperature. After another washing step, 30-μL droplets of the prepared 10× chiral NP solution were applied to each opening region and allowed to incubate for 1 h at room temperature. The chiral NPs with positive surface charges enable affixation of NPs to the final layer of anionic PSS on the pre-treated glass surface. (Figure 3C).

Surface modification of chiral NP for sEV isolation and sensing

After incubation, the excess unbound NP solution was rinsed off with DI water, and the devices were placed in 0.25 mM 11-mercaptoundecanoic acid (MUA) solution prepared in ultrapure ethanol for overnight incubation. To functionalize NeutrAvidin onto the glass surface, carbodiimide cross-linker chemistry was utilized. The devices were taken out of the MUA solution, washed with ethanol, and dried by carefully blowing air onto the surfaces. The MUA-modified surface of chiral Au NPs deposited onto slide glass was then modified by standard 1-ethyl-3-(3-dimethylaminopropyl) carbodiimide (EDC) and *N*-hydroxysuccinimide (NHS) chemistry, and Annexin V molecules were further immobilized on the NPs (Figure 3D). 100-μL droplets of 4 mM EDC solution prepared in DI water were applied to each sensing region and allowed to incubate for 30 min at room temperature. The excess EDC solution was then rinsed off with DI water, and 100-μL droplets of 8 mM sulfo-NHS solution (diluted in DI water from 50 mM stock) were applied and allowed to incubate for 30 min at room temperature. Each device was rinsed in DI water, and 100-μL droplets of 0.03 μM NeutrAvidin solution (diluted in PBS from 3 μM stock) were applied and allowed to incubate overnight at 4°C. When devices were needed for sample processing, they were taken out of the 4°C refrigerator, washed with PBS, and dried by carefully blowing air over the surfaces. 30-μL droplets of 10× diluted biotinylated Annexin V (diluted in calcium-rich 1× binding buffer) were applied and allowed to incubate for 40 min. This was followed by a wash with the 1× binding buffer, air drying, and CD signal reading as a baseline before the top PDMS layers were applied and samples processed.

Cell-culture- and cell-derived sEV preparation

As model samples, sEVs from two different lung cancer cell lines (A549 and H3255) and one lung fibroblast cell line (MRC5) were prepared. Lung cancer cell lines were cultured in serum-free medium for 3 days, and the cell-culture supernatant was centrifuged at 2,000 × *g* for 15 min; the resultant supernatant was followed by a second centrifugation at 12,000 × *g* to remove all residual cellular debris. The supernatant was then ultracentrifuged at 100,000 × *g* to isolate sEVs. We cultured each cell line in conditioned medium with exosome-depleted fetal bovine serum for 1–3 days, and the cell-culture supernatants were ultracentrifuged to isolate exosomes. After exosome separation, we measured the concentration of samples using NTA, and a known number of sEVs was used for model sample preparation.

Human plasma sample preparation

The clinical sample collection and experiments were approved by the Ethics and Institutional Review Board and Scientific Review Committee of the University of Michigan. Informed consent was obtained from all participants of this clinical study, and the blood samples of cancer patients were obtained after approval of the institutional review board at the University of Michigan (HUM00119934). All experiments were performed in accordance with the approved guidelines and regulations by the ethics committee at the University of Michigan. For plasma separation from whole blood, each blood sample was centrifuged using 5810R centrifuge (Eppendorf, Germany) at 2,000 × *g* for 15 min to sediment all nucleated cells, followed by a second centrifugation at 12,000 × *g* to remove all residual cellular debris. The clear supernatant from the second centrifugation was gently collected, filtered through a 200-nm syringe filter, and used throughout the study.

Sample preparation and on-chip processing

As the Annexin V-based sEV isolation is calcium dependent, model samples and plasma samples from patients were either prepared in a calcium-containing buffer or mixed with concentrated calcium-containing buffer solution (10×) prior to CDEXO experiments. For model samples, pre-isolated cell-derived sEVs were spiked into 30 μL of 1× binding buffer containing 2.5 mM $CaCl_2$. The plasma samples were also mixed with 10% plasma volume of 10× binding buffer accordingly so that the mixture had Ca^{2+} ion concentration equivalent to that of model samples. 30 μL of sample was injected to CDEXO chip through the inlet and incubated for 20 min. After sEV capture, 100 μL of 1× binding buffer was flowed through to remove excess unbound vesicles or protein debris in plasma, ensuring there was no biofouling that could potentially hinder the detection. For sEV release from the chip, 100 μL of 20 mM EDTA solution was flowed through, followed by injection of 100 μL of PBS buffer. The collected samples from the device underwent further NTA analysis depending on the study. In every step, CD spectra were obtained and analyzed.

Circular dichroism spectrometry

CD spectra were obtained using a Jasco J-815 CD spectrometer. A Jasco J-815 was also used for CD spectra measurement of model sEVs in a quartz cuvette. For the CDEXO chip experiment, the CD signal was taken in between each step of the sample-processing procedure, including baseline, post-capture, and post-release of sEVs. The baseline is indicative of the signal given off by the NPs, which are synthesized with L-cys on their surfaces as well as functionalized with the NeutrAvidin and Annexin V required to capture sEVs. The bulk of this baseline signal can be attributed to the optically active L-cys, although there were observable minimal shifts throughout the functionalization procedure that were monitored by CD spectroscopy. In every step, the CD spectra measurement was taken after removing the top PDMS layer of CDEXO, washing with buffer, and mild air drying. The bottom layer of the CDEXO chip was attached to the CD spectrometer insert using adhesive tape, and each measurement was conducted in triplicate.

Nanoparticle-tracking analysis of exosomes from cancer cells

For the evaluation of the concentration and the size distribution of the resultant effluent, NTA was performed using the NanoSight NS300 (Malvern Instruments, UK). For each measurement, 30 μL of the resultant was used and a laser module was mounted inside the main instrument housing. NTA visualizes the scattered light from the vesicles of interest based on their Brownian motion. This movement was monitored through a video sequence for 20 s in triplicate. All data acquisition and processing was performed using NanoSight NS300 control software (screen gain, 7; camera level, 13; detection threshold, 5), and concentration of particles in exosome sizes (30–150 nm) was used for calculating capture efficiencies of the present platform.

Electron microscopy imaging

Cryo-SEM analysis

The surface of CDEXO chip with or without sEV captured was examined by a Helios FIB scanning electron microscope with cryo-stage at −180°C under beam energies (2.0–5.0 kV) at the Michigan Center for Materials Characterization, University of Michigan. A cleaned silicon wafer was used as substrate. Directly after sEV capture experiments, the substrate was naturally dehydrated before being mounted on an SEM stub and imaged on the cryo-stage to reduce damage to the sEVs.

SEM and STEM imaging and analysis

The chiral NPs were deposited on TEM grid substrate for analysis of the same sample in SEM and TEM. For SEM images, we used a Helios FIB scanning electron microscope with beam energies (20 kV) at the Michigan Center for Materials Characterization at University of Michigan. A special TEM grid holder was utilized for SEM imaging. For STEM/TEM imaging and elemental mapping, a Thermo Fisher Talos 200X G2 scanning/transmission electron microscope equipped with Super-X windowless EDX detector was utilized. Velox software was utilized for image acquisition and analysis. For thiol group density analysis, we treated deposited NPs with only MUA. Further analysis of MUA density was confirmed with iron binding density on the NPs. For this analysis, we used 100 mM iron(III) chloride and applied 10 μL of suspension on the NP-deposited TEM grid. The grid was washed with Milli-Q water twice after 10 min.

Electromagnetic simulations for spatial light-matter interaction evaluation

The spatial maps of absorbance, scattering, and extinction (Figures S8 and S9) were collected using COMSOL Multiphysics and a similar method described in the section "numerical simulation of optical activities from chiral NPs." The 3D structure of NP with concave (diameter = 50 nm) at vertices (Figure 5C) was placed under both circularly polarized light (CPL) with the wavelength at 550 nm. The particle volume and surface integral of total energy dissipation density (E_{loss} [W/m^3])] and power outflow of the relative fields (P_{out} [W/m^2]) respectively represent absorbance and scattering by NPs. Thus, the two-dimensional plots for integral projection of E_{loss} ($Proj.E_{\text{loss}}$ [W/m^2]) and P_{out} on the surface of NPs, as well as their summation ($Proj.E_{\text{loss}} + P_{\text{out}}$) to evaluate total extinction, were collected under exposure to electromagnetic wave at resonance (Figure S8). The complex model with exosome-mimic dielectric particles was constructed with spherical particles of 24-nm radius and refractive index of 1.38, which corresponds to the refractive index of exosomes in the literature.[69]

The electric field formed that surrounded the chiral NP under the two different CPL sources (Figures 5F–5H and S10) and their differentiated field (Figure S11) were examined by generating volume plots of the high-field region; The plots were obtained for the field surpass a specific threshold condition for the air domain (with a refractive index of 1.0) in the chiral NP model on a substrate. The differential electric field was assessed by subtracting the field under the RCP configuration from the field under the LCP configuration.

Western blot analysis

RIPA buffer with 1% protease inhibitor was prepared for captured sEV lysis. The prepared buffer solution was applied to sEV samples. Total amount of proteins was measured by standard BCA analysis according to the manufacturer's instructions. Western blot analysis was performed on a precast 4%–20% SDS gel from Bio-Rad. The samples were prepared in 4× Laemmli buffer with 2-mercaptoethanol and heated to 90°C for 15 min before loading onto the gel. The gel was run at 120 V for 1 h before transferring at 120 V for 1 h 15 min on ice. Blocking was performed in 5% non-fat milk in TBST (Tris-buffered saline with Tween 20) for 90 min. Primary antibody was incubated overnight on a rocker at 4°C at a concentration of 1:1,000 in 3% non-fat milk in TBST. Thorough rinsing was performed before the secondary antibody was incubated for 90 min at room temperature (1:500 in 3% non-fat milk in TBST).

wOPD chirality indices of the mutant proteins

The weighted OPD (wOPD) chirality indices were computed for wild-type and mutation/deletion-expressed proteins. From each protein crystallography dataset (PDB files), we chose XYZ positions of α-carbon (C_α) to represent the protein structures, and the molecular weight of each residue was assigned to its corresponding C_α position. Considering that protein deletion and mutation are allowed to perturb the local protein structure, we adopted a coarse-grained method to find local chirality changes. At each individual residue, we discovered seven nearest-neighbor residues based on the Euclidean distance of the C_α position. The group of nearest residue positions is incorporated into the following equation to compute the wOPD chirality index.[53,63,70] In the following equation, w_x $(x = i, j, k, l)$ represents the molecular weight of each residue, r_{xy} $(x, y = i, j, k, l)$ is the vector composed of two points, x and y, and N stands for the number of points.

$$G_{\text{OS}} = \frac{4\,!}{N^4}\frac{1}{3}\left[\sum_{\substack{\text{all permunations of}\\ i,j,k,l\,=\,1\cdots N}} w_i w_j w_k w_l \times \frac{[(r_{ij} \times r_{kl}) \cdot r_{il}](r_{ij} \cdot r_{jk})(r_{jk} \cdot r_{kl})}{(r_{ij} r_{jk} r_{kl})^n {r_{il}}^m}\right].$$

The computed wOPD is assigned to each C_α position and averaged to find the overall chirality index for the entire structure of each protein at a certain condition.

Pocket analysis of chiral NPs

To analyze the pocket structure of NPs, we adopted the concept of minimum inaccessible radius, shell volume, and pocketness from Kawabata and Go.[71,72] The minimum inaccessible radius measures the radius of the circle that cannot reach the surface point of the NP. The shell volume enumerates the shallowness of the accessible surface of the NP. The pocketness represents the depth and size of concavity of the surface of the NP.[63,71,72] With the help of atomsk,[73] the 3D NP structure model is filled with FCC (face-centered cubic) Au supercells. The atomic coordinates are used for computing the minimum inaccessible radius, shell volume, and pocketness with the grid-based protein pocket and geometric surface detection software called *ghecom* (grid-based HECOMi finder)[71,72] in the Ubuntu 18.04 environment.

RNA extraction, cDNA synthesis, and RT-PCR

Different numbers of H3255 exosomes in 200 μL of PBS were prepared (10^2–10^8). RNA was purified from each of these samples using an in-house modified protocol using the Total Exosome RNA and Protein Isolation kit (cat. #4478545, Invitrogen, USA). In brief, 200 μL of exosome resuspension buffer (cat. #4478545, Invitrogen) was added and incubated for 5 min at room temperature, followed by the addition of denaturing solution (cat. #4478545, Invitrogen) that was pre-warmed to 37°C. After 5 min of incubation, 400 μL of acid-phenol/chloroform mixture (cat. #4478545, Invitrogen) was added, and the mixture was vortexed for 60 s followed by centrifugation at 14,000 × *g* for 10 min. The upper aqueous layer (RNA layer) was collected and mixed with 1.25× volume of 100% ethanol and added to the provided columns (cat. #4478545, Invitrogen After centrifuging at 14,000 × *g* for 1 min, the columns were washed once with wash solution 1 (cat. #4478545, Invitrogen) and twice with wash solution 2/3 (cat. #4478545, Invitrogen) and eluted into 20 μL of provided pre-heated (95°C) elution solution. The purified RNA was quantified using a NanoDrop ND-1000 Spectrophotometer (Thermo Scientific, USA) and then used to synthesize cDNA using SuperScript IV VILO with ezDNase Enzyme (cat. #11766050, Invitrogen). For qPCR, 100 μM stock of CD63 primer solution was self-prepared using forward and reverse primers (cat. #10336022, Invitrogen) and Milli-Q water. The qPCR mixture was prepared using 2 μL of the CD63 primer mix, 5 μL of SYBR Green ROX qPCR Mastermix (cat. #330523, Qiagen, USA), 1 μL of Milli-Q water, and 2 μL of cDNA. Finally, qPCR was performed in a MicroAmp Optical 384-well reaction plate (cat. #4326270) using Applied Biosystems QuantStudio 5 (A28570), and cycle threshold (Ct) values were noted for each concentration of exosomes.

Statistical analysis

All results are presented as mean ± standard deviation. Statistical analyses were conducted using GraphPad Prism software. Unpaired t tests (two-tailed) were performed to evaluate statistical significance between groups as explained below. When comparing capture efficiencies between healthy and cancer-derived sEVs, two groups were formed: group 1 comprises MRC5 and HD_exo, and group 2 comprises H1650, A549, and H3255. In contrast, when comparing capture efficiencies between Annexin V and EGFR, a two-group set was formed for each cell line (i.e., MRC5, A549, and H3255) where groups 1 and 2 comprised capture efficiency values from Annexin V and EGFR-functionalized devices, respectively. Similarly, to compare the performance of CDEXO chip with respect to ultracentrifugation, two-group sets were formed for each cell line (MRC5, H1650, A549, and H3255). Further, to compare peak shifts ($\Delta\lambda$) and percent changes of magnitude (ΔCD) in lung cancers vs. healthy control-derived sEVs, multiple two-group sets were formed with group 2 comprising one cancer cell line (H1650, A549, or H3255) and group 1 comprising MRC5. The same statistical test was used for magnitude change and percent change comparison in EGFR deletion/mutation subgroups. ANOVA test was performed using RStudio (version 4.2.1). In brief, a table with patient information was imported as a .csv file and the function aov( ) was used to obtain a summary of the test. The following groups were used: sex, stage (IA, III, IV, N/A), adenocarcinoma type (ALK, EGFR, ROS1, squamous cell), mutation (EGFR exon 19 deletion, exon 19 deletion + T790M, EGFR mutant with T790M, EGFR mutation, L858R, ROS-1, ROS-1 rearrangement, and none), treatment (afatinib + cetuximab, carboplatin + paclitaxel + radiation, carboplatin + pemetrexed, pemetrexed, tyrosine kinase inhibitors), and tumor origin (neck, lymph node, left or right upper lobe, left or right lower lobe).

Statistical significance was defined when $p < 0.05$ was obtained.

RESOURCE AVAILABILITY

Lead contact

The lead contact for this paper is Sunitha Nagrath (snagrath@umich.edu).

Materials availability

Samples of the chiral Au NPs used in this study are available upon request from the Kotov lab at University of Michigan.

Data and code availability

The authors declare that all data supporting the findings of this study are available within the paper and its supplemental information. The raw and analyzed datasets generated during the study are available for research purposes from the corresponding authors upon reasonable request.

ACKNOWLEDGMENTS

The authors thank the Dipankar Ray lab at the University of Michigan for their generous gift of the H3255 lung cancer cell line. The authors also acknowledge the financial support of the University of Michigan College of Engineering and NSF grant #DMR-0320740, and technical support from the Michigan Center for Materials Characterization. This work was supported by grants from National Institutes of Health (NIH), 5-R33-CA-202867-02 and 1-R01-CA-208335-01-A1 to S.N., and support from Forbes Institute for Cancer Discovery at University of Michigan. A part of this work was supported by Vannevar Bush DoD Fellowship to N.A.K. titled, “Engineered Chiral Ceramics” ONR N000141812876. The authors are also grateful for the financial support from NSF grant #2317423 "Lock-and-Key Interactions of Proteins and Chiral Nanoparticles" and grant #2243104, Center for Complex Particle Systems (COMPASS). Michigan Center for Materials Characterization is acknowledged for its assistance with electron microscopy, and for the NSF grant #DMR-9871177 for funding of the JEOL 2010F analytical electron microscope used in this work. Y.-T.K. is an Innovation Fellow supported by Biointerfaces Institute, University of Michigan.

AUTHOR CONTRIBUTIONS

Y.-T.K., S.N., and N.A.K. designed the original research. Y.-T.K., J.-Y.K., E.S.T.-E., and C.P.-R. conducted experiments and analyzed the data. J.-Y.K. and H.-J.J. designed chiral gold NPs and their deposition method. J.-Y.K., H.-J.J., and C.-M.L. synthesized chiral gold NPs. J.-Y.K. performed tomography and NP-sEV simulation. J.-Y.K., E.S.T.-E., Y.-T.K., and A.K. prepared electron microscopy specimens, and J.-Y.K. and E.S.T.-E. performed electron microscopy. M.C., E.S.T.-E., and J.-Y.K. performed wOPD chirality indices calculation. A.K., E.P., and C.S. analyzed western blot analysis and cell characterization. A.K. and S.O. prepared normal and cancerous lung cancer cell culture and EV harvest. A.K. and E.P. conducted ultracentrifugation for model sample preparation. R.R., S.J., and N.R. recruited patients and provided cancer patients’ plasma samples as well as clinical data. Y.-T.K., J.-Y.K., S.N., and N.A.K. wrote the manuscript.

DECLARATION OF INTERESTS

The authors declare no competing interests.

SUPPLEMENTAL INFORMATION

Supplemental information can be found online at https://doi.org/10.1016/j.matt.2024.09.005.

Received: December 13, 2023
Revised: June 18, 2024
Accepted: September 6, 2024
Published: September 27, 2024

REFERENCES

1. van Niel, G., D’Angelo, G., and Raposo, G. (2018). Shedding light on the cell biology of extracellular vesicles. Nat. Rev. Mol. Cell Biol. *19*, 213–228. https://doi.org/10.1038/nrm.2017.125.
2. Thery, C., Zitvogel, L., and Amigorena, S. (2002). Exosomes: composition, biogenesis and function. Nat. Rev. Immunol. *2*, 569–579. https://doi.org/10.1038/nri855.
3. Zhang, Y., Liu, Y., Liu, H., and Tang, W.H. (2019). Exosomes: biogenesis, biologic function and clinical potential. Cell Biosci. *9*, 19. https://doi.org/10.1186/s13578-019-0282-2.
4. Hoshino, A., Costa-Silva, B., Shen, T.L., Rodrigues, G., Hashimoto, A., Tesic Mark, M., Molina, H., Kohsaka, S., Di Giannatale, A., Ceder, S., et al. (2015). Tumour exosome integrins determine organotropic metastasis. Nature *527*, 329–335. https://doi.org/10.1038/nature15756.
5. Yang, Y., Hong, Y., Cho, E., Kim, G.B., and Kim, I.S. (2018). Extracellular vesicles as a platform for membrane-associated therapeutic protein delivery. J. Extracell. Vesicles *7*, 1440131. https://doi.org/10.1080/20013078.2018.1440131.
6. Azmi, A.S., Bao, B., and Sarkar, F.H. (2013). Exosomes in cancer development, metastasis, and drug resistance: a comprehensive review. Cancer Metastasis Rev. *32*, 623–642. https://doi.org/10.1007/s10555-013-9441-9.
7. Wortzel, I., Dror, S., Kenific, C.M., and Lyden, D. (2019). Exosome-Mediated Metastasis: Communication from a Distance. Dev. Cell *49*, 347–360. https://doi.org/10.1016/j.devcel.2019.04.011.
8. Purcell, E., Owen, S., Prantzalos, E., Radomski, A., Carman, N., Lo, T.W., Zeinali, M., Subramanian, C., Ramnath, N., and Nagrath, S. (2021). Epidermal Growth Factor Receptor Mutations Carried in Extracellular Vesicle-Derived Cargo Mirror Disease Status in Metastatic Non-small Cell Lung Cancer. Front. Cell Dev. Biol. *9*, 724389. https://doi.org/10.3389/fcell.2021.724389.
9. Tan, X., Lambert, P.F., Rapraeger, A.C., and Anderson, R.A. (2016). Stress-Induced EGFR Trafficking: Mechanisms, Functions, and Therapeutic Implications. Trends Cell Biol. *26*, 352–366. https://doi.org/10.1016/j.tcb.2015.12.006.
10. Vlassov, A.V., Magdaleno, S., Setterquist, R., and Conrad, R. (2012). Exosomes: current knowledge of their composition, biological functions, and diagnostic and therapeutic potentials. Biochim. Biophys. Acta *1820*, 940–948. https://doi.org/10.1016/j.bbagen.2012.03.017.
11. Shao, H., Im, H., Castro, C.M., Breakefield, X., Weissleder, R., and Lee, H. (2018). New Technologies for Analysis of Extracellular Vesicles. Chem. Rev. *118*, 1917–1950. https://doi.org/10.1021/acs.chemrev.7b00534.
12. Onukwugha, N.E., Kang, Y.T., and Nagrath, S. (2022). Emerging micro-nanotechnologies for extracellular vesicles in immuno-oncology: from target specific isolations to immunomodulation. Lab Chip *22*, 3314–3339. https://doi.org/10.1039/d2lc00232a.
13. Li, P., Kaslan, M., Lee, S.H., Yao, J., and Gao, Z. (2017). Progress in Exosome Isolation Techniques. Theranostics *7*, 789–804. https://doi.org/10.7150/thno.18133.
14. Zhang, Y., Bi, J., Huang, J., Tang, Y., Du, S., and Li, P. (2020). Exosome: A Review of Its Classification, Isolation Techniques, Storage, Diagnostic and Targeted Therapy Applications. Int. J. Nanomed. *15*, 6917–6934. https://doi.org/10.2147/IJN.S264498.
15. Chen, J., Li, P., Zhang, T., Xu, Z., Huang, X., Wang, R., and Du, L. (2021). Review on Strategies and Technologies for Exosome Isolation and Purification. Front. Bioeng. Biotechnol. *9*, 811971. https://doi.org/10.3389/fbioe.2021.811971.
16. Kang, Y.T., Hadlock, T., Jolly, S., and Nagrath, S. (2020). Extracellular vesicles on demand (EVOD) chip for screening and quantification of cancer-associated extracellular vesicles. Biosens. Bioelectron. *168*, 112535. https://doi.org/10.1016/j.bios.2020.112535.
17. Reategui, E., van der Vos, K.E., Lai, C.P., Zeinali, M., Atai, N.A., Aldikacti, B., Floyd, F.P., Jr., A, H.K., Thapar, V., Hochberg, F.H., et al. (2018). Engineered nanointerfaces for microfluidic isolation and molecular profiling of tumor-specific extracellular vesicles. Nat. Commun. *9*, 175. https://doi.org/10.1038/s41467-017-02261-1.

18. Zhao, Z., Yang, Y., Zeng, Y., and He, M. (2016). A microfluidic ExoSearch chip for multiplexed exosome detection towards blood-based ovarian cancer diagnosis. Lab Chip *16*, 489–496. https://doi.org/10.1039/c5lc01117e.
19. Pires, N.M.M., Dong, T., Hanke, U., and Hoivik, N. (2014). Recent developments in optical detection technologies in lab-on-a-chip devices for biosensing applications. Sensors *14*, 15458–15479. https://doi.org/10.3390/s140815458.
20. Jahn, I.J., Žukovskaja, O., Zheng, X.S., Weber, K., Bocklitz, T.W., Cialla-May, D., and Popp, J. (2017). Surface-enhanced Raman spectroscopy and microfluidic platforms: challenges, solutions and potential applications. Analyst *142*, 1022–1047. https://doi.org/10.1039/c7an00118e.
21. Liu, C., Zeng, X., An, Z., Yang, Y., Eisenbaum, M., Gu, X., Jornet, J.M., Dy, G.K., Reid, M.E., Gan, Q., and Wu, Y. (2018). Sensitive Detection of Exosomal Proteins via a Compact Surface Plasmon Resonance Biosensor for Cancer Diagnosis. ACS Sens. *3*, 1471–1479. https://doi.org/10.1021/acssensors.8b00230.
22. Qiu, G., Thakur, A., Xu, C., Ng, S.-P., Lee, Y., and Wu, C.-M.L. (2019). Detection of Glioma-Derived Exosomes with the Biotinylated Antibody-Functionalized Titanium Nitride Plasmonic Biosensor. Adv. Funct. Mater. *29*, 1806761. https://doi.org/10.1002/adfm.201806761.
23. Cheng, N., Du, D., Wang, X., Liu, D., Xu, W., Luo, Y., and Lin, Y. (2019). Recent advances in biosensors for detecting cancer-derived exosomes. Trends Biotechnol. *37*, 1236–1254. https://doi.org/10.1016/j.tibtech.2019.04.008.
24. Tokel, O., Yildiz, U.H., Inci, F., Durmus, N.G., Ekiz, O.O., Turker, B., Cetin, C., Rao, S., Sridhar, K., Natarajan, N., et al. (2015). Portable microfluidic integrated plasmonic platform for pathogen detection. Sci. Rep. *5*, 9152. https://doi.org/10.1038/srep09152.
25. Reza, K.K., Sina, A.A.I., Wuethrich, A., Grewal, Y.S., Howard, C.B., Korbie, D., and Trau, M. (2019). A SERS microfluidic platform for targeting multiple soluble immune checkpoints. Biosens. Bioelectron. *126*, 178–186. https://doi.org/10.1016/j.bios.2018.10.044.
26. Kwizera, E.A., O'Connor, R., Vinduska, V., Williams, M., Butch, E.R., Snyder, S.E., Chen, X., and Huang, X. (2018). Molecular detection and analysis of exosomes using surface-enhanced Raman scattering gold nanorods and a miniaturized device. Theranostics *8*, 2722–2738. https://doi.org/10.7150/thno.21358.
27. Shin, H., Choi, B.H., Shim, O., Kim, J., Park, Y., Cho, S.K., Kim, H.K., and Choi, Y. (2023). Single test-based diagnosis of multiple cancer types using Exosome-SERS-AI for early stage cancers. Nat. Commun. *14*, 1644. https://doi.org/10.1038/s41467-023-37403-1.
28. Wang, Z., Zong, S., Wang, Y., Li, N., Li, L., Lu, J., Wang, Z., Chen, B., and Cui, Y. (2018). Screening and multiple detection of cancer exosomes using an SERS-based method. Nanoscale *10*, 9053–9062. https://doi.org/10.1039/c7nr09162a.
29. Park, J., Hwang, M., Choi, B., Jeong, H., Jung, J.-H., Kim, H.K., Hong, S., Park, J.-H., and Choi, Y. (2017). Exosome classification by pattern analysis of surface-enhanced Raman spectroscopy data for lung cancer diagnosis. Anal. Chem. *89*, 6695–6701. https://doi.org/10.1021/acs.analchem.7b00911.
30. Shin, H., Jeong, H., Park, J., Hong, S., and Choi, Y. (2018). Correlation between cancerous exosomes and protein markers based on surface-enhanced Raman spectroscopy (SERS) and principal component analysis (PCA). ACS Sens. *3*, 2637–2643. https://doi.org/10.1021/acssensors.8b01047.
31. Shin, H., Oh, S., Hong, S., Kang, M., Kang, D., Ji, Y.-G., Choi, B.H., Kang, K.-W., Jeong, H., Park, Y., et al. (2020). Early-stage lung cancer diagnosis by deep learning-based spectroscopic analysis of circulating exosomes. ACS Nano *14*, 5435–5444. https://doi.org/10.1021/acsnano.9b09119.
32. Im, H., Shao, H., Park, Y.I., Peterson, V.M., Castro, C.M., Weissleder, R., and Lee, H. (2014). Label-free detection and molecular profiling of exosomes with a nano-plasmonic sensor. Nat. Biotechnol. *32*, 490–495. https://doi.org/10.1038/nbt.2886.
33. Bellassai, N., D'Agata, R., Jungbluth, V., and Spoto, G. (2019). Surface plasmon resonance for biomarker detection: Advances in non-invasive cancer diagnosis. Front. Chem. *7*, 570. https://doi.org/10.3389/fchem.2019.00570.
34. Chen, W., Bian, A., Agarwal, A., Liu, L., Shen, H., Wang, L., Xu, C., and Kotov, N.A. (2009). Nanoparticle superstructures made by polymerase chain reaction: collective interactions of nanoparticles and a new principle for chiral materials. Nano Lett. *9*, 2153–2159. https://doi.org/10.1021/nl900726s.
35. Valev, V.K., Baumberg, J.J., Sibilia, C., and Verbiest, T. (2013). Chirality and chiroptical effects in plasmonic nanostructures: fundamentals, recent progress, and outlook. Adv. Mater. *25*, 2517–2534. https://doi.org/10.1002/adma.201205178.
36. Liu, Y., Wu, Z., Armstrong, D.W., Wolosker, H., and Zheng, Y. (2023). Detection and analysis of chiral molecules as disease biomarkers. Nat. Rev. Chem *7*, 355–373. https://doi.org/10.1038/s41570-023-00476-z.
37. Tsochantaris, E., Muthachikavil, A.V., Peng, B., Liang, X., and Kontogeorgis, G.M. (2022). Multiple insights call for revision of modern thermodynamic models to account for structural fluctuations in water. AIChE J. *68*, e17891. https://doi.org/10.1002/aic.17891.
38. Miles, A.J., and Wallace, B.A. (2016). Circular dichroism spectroscopy of membrane proteins. Chem. Soc. Rev. *45*, 4859–4872. https://doi.org/10.1039/c5cs00084j.
39. Whitmore, L., and Wallace, B.A. (2008). Protein secondary structure analyses from circular dichroism spectroscopy: methods and reference databases. Biopolymers *89*, 392–400. https://doi.org/10.1002/bip.20853.
40. Wu, X., Xu, L., Liu, L., Ma, W., Yin, H., Kuang, H., Wang, L., Xu, C., and Kotov, N.A. (2013). Unexpected chirality of nanoparticle dimers and ultrasensitive chiroplasmonic bioanalysis. J. Am. Chem. Soc. *135*, 18629–18636. https://doi.org/10.1021/ja4095445.
41. Sun, M., Xu, L., Bahng, J.H., Kuang, H., Alben, S., Kotov, N.A., and Xu, C. (2017). Intracellular localization of nanoparticle dimers by chirality reversal. Nat. Commun. *8*, 1847. https://doi.org/10.1038/s41467-017-01337-2.
42. Xu, L., Wang, X., Wang, W., Sun, M., Choi, W.J., Kim, J.-Y., Hao, C., Li, S., Qu, A., Lu, M., et al. (2022). Enantiomer-dependent immunological response to chiral nanoparticles. Nature *601*, 366–373. https://doi.org/10.1038/s41586-021-04243-2.
43. Di Capua, D., Bracken-Clarke, D., Ronan, K., Baird, A.-M., and Finn, S. (2021). The liquid biopsy for lung cancer: State of the art, limitations and future developments. Cancers *13*, 3923. https://doi.org/10.3390/cancers13163923.
44. Liu, Y., Wang, J., Xiong, Q., Hornburg, D., Tao, W., and Farokhzad, O.C. (2021). Nano-bio interactions in cancer: From therapeutics delivery to early detection. Acc. Chem. Res. *54*, 291–301. https://doi.org/10.1021/acs.accounts.0c00413.
45. Zhao, Y., Xu, L., Ma, W., Wang, L., Kuang, H., Xu, C., and Kotov, N.A. (2014). Shell-engineered chiroplasmonic assemblies of nanoparticles for zeptomolar DNA detection. Nano Lett. *14*, 3908–3913. https://doi.org/10.1021/nl501166m.
46. Kumar, J., Eraña, H., López-Martínez, E., Claes, N., Martín, V.F., Solís, D.M., Bals, S., Cortajarena, A.L., Castilla, J., and Liz-Marzán, L.M. (2018). Detection of amyloid fibrils in Parkinson's disease using plasmonic chirality. Proc. Natl. Acad. Sci. USA *115*, 3225–3230. https://doi.org/10.1073/pnas.1721690115.
47. Šťovíčková, L., Tatarkovič, M., Logerová, H., Vavřinec, J., and Setnička, V. (2015). Identification of spectral biomarkers for type 1 diabetes mellitus using the combination of chiroptical and vibrational spectroscopy. Analyst *140*, 2266–2272. https://doi.org/10.1039/c4an01874e.
48. Kotov, N.A., Magonov, S., and Tropsha, E. (1998). Layer-by-layer self-assembly of Alumosilicate−Polyelectrolyte composites: Mechanism of deposition, crack resistance, and perspectives for novel membrane materials. Chem. Mater. *10*, 886–895. https://doi.org/10.1021/cm970649b.

49. Boada, C.A., Zinger, A., Rohen, S., Martinez, J.O., Evangelopoulos, M., Molinaro, R., Lu, M., Villarreal-Leal, R.A., Giordano, F., Sushnitha, M., et al. (2021). LDL-based lipid nanoparticle derived for blood plasma accumulates preferentially in atherosclerotic plaque. Front. Bioeng. Biotechnol. *9*, 794676. https://doi.org/10.3389/fbioe.2021.794676.
50. Kang, Y.-T., Purcell, E., Palacios-Rolston, C., Lo, T.-W., Ramnath, N., Jolly, S., and Nagrath, S. (2019). Isolation and Profiling of Circulating Tumor-Associated Exosomes Using Extracellular Vesicular Lipid-Protein Binding Affinity Based Microfluidic Device. Small *15*, e1903600. https://doi.org/10.1002/smll.201903600.
51. Nakai, W., Yoshida, T., Diez, D., Miyatake, Y., Nishibu, T., Imawaka, N., Naruse, K., Sadamura, Y., and Hanayama, R. (2016). A novel affinity-based method for the isolation of highly purified extracellular vesicles. Sci. Rep. *6*, 33935. https://doi.org/10.1038/srep33935.
52. Lee, H.-E., Ahn, H.-Y., Mun, J., Lee, Y.Y., Kim, M., Cho, N.H., Chang, K., Kim, W.S., Rho, J., and Nam, K.T. (2018). Amino-acid- and peptide-directed synthesis of chiral plasmonic gold nanoparticles. Nature *556*, 360–365. https://doi.org/10.1038/s41586-018-0034-1.
53. Kim, J.-Y., Yeom, J., Zhao, G., Calcaterra, H., Munn, J., Zhang, P., and Kotov, N. (2019). Assembly of gold nanoparticles into chiral superstructures driven by circularly polarized light. J. Am. Chem. Soc. *141*, 11739–11744. https://doi.org/10.1021/jacs.9b00700.
54. Qu, A., Sun, M., Kim, J.-Y., Xu, L., Hao, C., Ma, W., Wu, X., Liu, X., Kuang, H., Kotov, N.A., and Xu, C. (2021). Stimulation of neural stem cell differentiation by circularly polarized light transduced by chiral nanoassemblies. Nat. Biomed. Eng. *5*, 103–113. https://doi.org/10.1038/s41551-020-00634-4.
55. Iost, R.M., and Crespilho, F.N. (2012). Layer-by-layer self-assembly and electrochemistry: applications in biosensing and bioelectronics. Biosens. Bioelectron. *31*, 1–10. https://doi.org/10.1016/j.bios.2011.10.040.
56. Kotov, N.A. (2001). Ordered layered assemblies of nanoparticles. MRS Bull. *26*, 992–997. https://doi.org/10.1557/mrs2001.255.
57. Mariani, S., Robbiano, V., Strambini, L.M., Debrassi, A., Egri, G., Dähne, L., and Barillaro, G. (2018). Layer-by-layer biofunctionalization of nanostructured porous silicon for high-sensitivity and high-selectivity label-free affinity biosensing. Nat. Commun. *9*, 5256. https://doi.org/10.1038/s41467-018-07723-8.
58. Zhao, S., Caruso, F., Dähne, L., Decher, G., De Geest, B.G., Fan, J., Feliu, N., Gogotsi, Y., Hammond, P.T., Hersam, M.C., et al. (2019). The future of layer-by-layer assembly: A tribute to ACS nano associate editor Helmuth Möhwald. ACS Nano *13*, 6151–6169. https://doi.org/10.1021/acsnano.9b03326.
59. Kotov, N.A., Dékány, I., and Fendler, J.H. (1996). Ultrathin graphite oxide–polyelectrolyte composites prepared by self-assembly: Transition between conductive and non-conductive states. Adv. Mater. *8*, 637–641. https://doi.org/10.1002/adma.19960080806.
60. Stone, H.A., Stroock, A.D., and Ajdari, A. (2004). Engineering flows in small devices: Microfluidics toward a lab-on-a-chip. Annu. Rev. Fluid Mech. *36*, 381–411. https://doi.org/10.1146/annurev.fluid.36.050802.122124.
61. Wang, G., Li, K., Purcell, F.J., Zhao, D., Zhang, W., He, Z., Tan, S., Tang, Z., Wang, H., and Reichmanis, E. (2016). Three-dimensional clustered nanostructures for microfluidic surface-enhanced Raman detection. ACS Appl. Mater. Interfaces *8*, 24974–24981. https://doi.org/10.1021/acsami.6b10542.
62. Marvar, J., Kumari, A., Onukwugha, N.-E., Achreja, A., Meurs, N., Animasahun, O., Roy, J., Paserba, M., Raju, K.S., Fortna, S., et al. (2023). Porous PDMS-based microsystem (ExoSponge) for rapid cost-effective tumor extracellular vesicle isolation and mass spectrometry-based metabolic biomarker screening. Adv. Mater. Technol. *8*, 2201937. https://doi.org/10.1002/admt.202201937.
63. Cha, M., Emre, E.S.T., Xiao, X., Kim, J.-Y., Bogdan, P., VanEpps, J.S., Violi, A., and Kotov, N.A. (2022). Unifying structural descriptors for biological and bioinspired nanoscale complexes. Nat. Comput. Sci. *2*, 243–252. https://doi.org/10.1038/s43588-022-00229-w.
64. Kumar, P., Vo, T., Cha, M., Visheratina, A., Kim, J.-Y., Xu, W., Schwartz, J., Simon, A., Katz, D., Nicu, V.P., et al. (2023). Photonically active bowtie nanoassemblies with chirality continuum. Nature *615*, 418–424. https://doi.org/10.1038/s41586-023-05733-1.
65. Liu, Y., Wu, Z., Kollipara, P.S., Montellano, R., Sharma, K., and Zheng, Y. (2021). Label-free ultrasensitive detection of abnormal chiral metabolites in diabetes. ACS Nano *15*, 6448–6456. https://doi.org/10.1021/acsnano.0c08822.
66. He, M., Crow, J., Roth, M., Zeng, Y., and Godwin, A.K. (2014). Integrated immunoisolation and protein analysis of circulating exosomes using microfluidic technology. Lab Chip *14*, 3773–3780. https://doi.org/10.1039/c4lc00662c.
67. Millstone, J.E., Métraux, G.S., and Mirkin, C.A. (2006). Controlling the edge length of gold nanoprisms via a seed-mediated approach. Adv. Funct. Mater. *16*, 1209–1214. https://doi.org/10.1002/adfm.200600066.
68. Johnson, P.B., and Christy, R.W. (1972). Optical constants of the noble metals. Phys. Rev. B *6*, 4370–4379. https://doi.org/10.1103/physrevb.6.4370.
69. Rupert, D.L.M., Mapar, M., Shelke, G.V., Norling, K., Elmeskog, M., Lötvall, J.O., Block, S., Bally, M., Agnarsson, B., and Höök, F. (2018). Effective refractive index and lipid content of extracellular vesicles revealed using optical waveguide scattering and fluorescence microscopy. Langmuir *34*, 8522–8531. https://doi.org/10.1021/acs.langmuir.7b04214.
70. Osipov, M.A., Pickup, B.T., and Dunmur, D.A. (1995). A new twist to molecular chirality: intrinsic chirality indices. Mol. Phys. *84*, 1193–1206. https://doi.org/10.1080/00268979500100831.
71. Kawabata, T. (2010). Detection of multiscale pockets on protein surfaces using mathematical morphology. Proteins *78*, 1195–1211. https://doi.org/10.1002/prot.22639.
72. Kawabata, T., and Go, N. (2007). Detection of pockets on protein surfaces using small and large probe spheres to find putative ligand binding sites. Proteins *68*, 516–529. https://doi.org/10.1002/prot.21283.
73. Hirel, P. (2015). Atomsk: A tool for manipulating and converting atomic data files. Comput. Phys. Commun. *197*, 212–219. https://doi.org/10.1016/j.cpc.2015.07.012.